Solar Cooling Systems

Y. F. Xu, Ming Li, Y. F. Wang, and Ruzhu Wang

Contents

Abstract

Due to a large amount of greenhouse gas emissions caused by burning traditional fossil energy resources, the environmental temperature has increased year by year, which has led to the yearly increase in the demand for air-conditioning. However, the conventional air-conditionings driven by grid power are the main

Y. F. Xu
Zhejiang Solar Energy Product Quality Inspection Center, Zhejiang, China

Solar Energy Research Institute, Yunnan Normal University, Kunming, China

M. Li (✉) · Y. F. Wang
Solar Energy Research Institute, Yunnan Normal University, Kunming, China
e-mail: lmllldy@126.com

R. Wang
Institute of Refrigeration and Cryogenies, School of Mechanical Engineering, Shanghai Jiao Tong University, Shanghai, China

R. Wang, X. Zhai (eds.), *Handbook of Energy Systems in Green Buildings*,
https://doi.org/10.1007/978-3-662-49120-1_33

products in the global market. Besides, using electric air-conditioning increases electrical pressure in peak times. In order to alleviate the contradiction between power demand and supply, more thermal power stations have been built, and more fossil fuels have been burnt in the past decades. In this context, more greenhouse gas has been discharged, and a vicious cycle has emerged between power generation and greenhouse gas emissions. Therefore, the refrigeration driven by solar energy has become one of the promising approaches to reduce or partially replace conventional refrigeration systems under the pressure of environmental protection. Solar thermal refrigeration and solar photovoltaic refrigeration are two main refrigeration modes in the field of solar refrigeration.

Under this background, a solar-powered adsorption cooling system was designed and optimized. The performance test results show that its maximum cooling efficiency was 0.122, and it could make 6.5 kg of ice at most daily. The cooling efficiency of the solar-powered adsorption refrigeration system with valve control in the adsorption/desorption process was significantly higher than that without valve control. A 23 kW single-effect LiBr-H_2O absorption chiller driven by PTC was investigated as well. The results reveal that its average refrigeration coefficient $\eta_{r,av}$ was between 0.18 and 0.60, and the average coefficient of performance (COP) of the whole refrigeration cycle $COP_{s,av}$ was between 0.11 and 0.27 under different weather conditions. In the mode of photovoltaic refrigeration, PV refrigerator and PV air-conditioning system were studied through experiments. PV refrigerator was mainly powered by photovoltaic module on sunny days and battery bank on overcast days. When the freezing room of the refrigerator was crammed with 5 kg, 6 kg, and 7 kg of water, the COP of this system was 0.24, 0.29, and 0.34, respectively. The 1.5 HP steam compression air-conditioning driven by PV array was built, and a 1-year investigation on its operation performance was made through an experiment. The research results indicate that the 1.5 HP steam compression type air-conditioning could be independently driven by PV array when solar irradiance was higher than 675 W/m^2. On sunny days, the air-conditioning system could be completely driven by PV array for about 4 h per day. All its daily average COPs were about 0.35, and daily average guarantee rates were between 0.93 and 1.25.

Keywords
Solar cooling · Adsorption cooling · Absorption cooling · PV refrigerator · PV air-conditioning · Coefficient of performance (COP) · Battery bank · PV array · System guarantee rate

Introduction of Solar Cooling System

Background

With the development of economy and the improvement of living standard, the cooling demand of people has increased continuously, especially in hot summers. Consequently, there is a shortage of electric power supply in cities, and the

phenomenon of power blackouts still happens. To ease the tension between electric supply and demand, the governments of all countries have taken measures. On the one hand, they have formulated specific electricity policies, tariff structures, and other preferential policies to encourage the use of electricity at night. On the other hand, they have improved the capacity of thermal power generation year by year to meet the increasing power demand in industrial production and people's lives. Nevertheless, the fossil fuels in conventional energy sources have been excessively exploited. Under this condition, large amounts of greenhouse gas and harmful particles have been emitted. The climate and the environment have been greatly damaged. According to statistics, when 10,000 kWh of electricity is generated in thermal power plants, the emission amounts of CO_2, SO_2, NO_x, and dust are 42.8 kiloton, 131 ton, 122 ton, and 20 ton, respectively. Even after the installation of efficient dust removal facilities, the PM2.5 particles still account for about 80% of the smoke emitted from thermal power plants. The research results show that the burning of large amounts of fossil fuels has caused the global average temperature to increase by 0.3–0.6° over the past 100 years and the sea level to rise by an average of 10–25 cm. If greenhouse gases cannot be reduced, the global average temperature will rise by 0.2° every 10 years. The excessive use of fossil fuels leads to serious air pollution and causes the concentration of PM2.5 seriously to exceed the standard. According to the Global Environment Outlook 5 (GEO-5) released by the United Nations Environment Programme in 2012, about two million of the world's premature deaths are related to PM2.5 pollutants [1].

Under the double pressure of energy shortage and air pollution, it has become a new normal thing to realize the rational adjustment and sustainable utilization of energy structure and increase the development and effective utilization of renewable energy. Among so many kinds of renewable energy, solar energy has many advantages, such as abundant resources, environment friendliness, and harmlessness to ecological balance. As a result, solar energy has become one of the most important parts of new energy and renewable energy utilization over the world. As the change of solar energy with time and space matches well with the cooling demand, the cooling system driven by solar energy has become a hot research topic, which can effectively alleviate the contradiction between power supply and demand. From the perspective of efficient energy utilization and environmental protection, solar-driven new cooling is one of the most promising solar energy utilization methods. For these reasons, it is an urgent task to study and improve the performance of solar cooling system in depth.

Classification of Solar Thermal Cooling System

The solar cooling systems under study have various cooling modes, which mainly include solar thermal cooling and solar photovoltaic cooling modes [2, 3]. The working principle of solar thermal cooling is as follows: the cooling system is driven by the heat transfer medium heated by the thermal energy collected from solar irradiance with adsorption cooling, absorption cooling, jet cooling, and other cooling methods. Solar photovoltaic cooling is a cooling mode. Under this mode, cooling

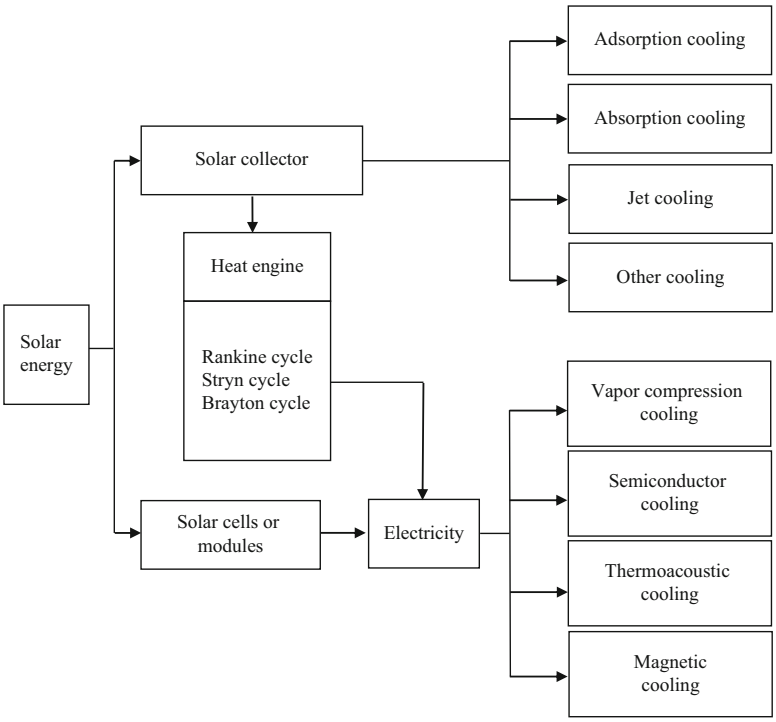

Fig. 1 Classification of solar cooling system

unit is driven by the electricity converted from solar energy by the PV modules. The cooling system mainly has steam compression cooling, semiconductor cooling, thermoacoustic cooling, and magnetic cooling modes. The refrigerator is also driven by the electricity generated by the heat engine, which is driven by the thermal energy collected by the solar collector. The classification of solar cooling is shown in Fig. 1.

Solar Thermal Cooling

Background

Solar thermal cooling includes adsorption cooling and absorption cooling, which is driven by the thermal energy collected from the sun. The researches of the solar-powered adsorption cooling technology mainly concentrate on three aspects, namely the improvement of the performances of the adsorption working pairs [4, 5], the development of the composite adsorbents with excellent heat transfer characterizations, and the optimization of the absorbent bed structures for achieving heat and mass transfer enhancement [6, 7] in the solar-powered solid adsorption cooling system. In

addition, numerous studies have been made by scholars at home and abroad to improve cooling efficiency, increase the stability and reliability of system operation, optimize the structure of cooling equipment, and select working pairs [8–15].

Common adsorption working pairs include active carbon-methanol [16], molecular sieve-water, silica gel-water [17], activated carbon-ammonia [18], calcium chloride-ammonia, etc. [19, 20]. Their adsorption types may be divided into physical adsorption and chemical adsorption. Physical adsorption working pairs usually prefer solar energy as the heat source. Zeolite-water, activated carbon-ammonia, and calcium chlorides-ammonia working pairs are suitable for high temperature waste heat utilizations. The adsorption heat for zeolite-water pair is about 3300–4200 kJ/kg. Zeolite-water pair is stable at high temperatures. It can have higher coefficient of performance (COP) and system cooling power unit mass adsorbents (SCP), if the temperature of the heat source is higher than 200 °C. Silica gel-water and activated carbon-methanol working pairs are suitable for solar energy due to their low desorption temperatures. Researchers from Japan [21, 22] and China [23, 24] have developed their adsorption systems using silica gel-water as the working pair. The systems could be powered by a heat source at a temperature of 50 °C and 55 °C, respectively. The disadvantages of the silica gel-water working pair include low adsorption quantity (0.2 kg/kg), and the only suitability for air-conditioning due to the impossibility to produce subzero temperature. Activated carbon-methanol pair can be used for freezing applications. As considered by Critoph and Vogel [25] and Meunier [26], the desorption temperature of the activated carbon-methanol working pair is around 100 °C, which well matches the temperature of the driving thermal source from solar energy. At that temperature, a large amount of methanol would be desorbed. Meanwhile, a high solar radiation collecting efficiency could be reached. Additionally, the evaporation latent heat of methanol is up to 1100 kJ/kg, which is beneficial to system miniaturization. These are great advantages for the application of such working pair in the solar-powered intermittent solid adsorption cooling system.

Absorption and adsorption are comparable, since adsorption chillers are more expensive and bulkier than absorption chillers. The total cost of a single-effect LiBr-H_2O absorption system is estimated to be the lowest [27]. In this case, numerous studies have been made on the solar absorption cooling system using single-effect LiBr-H_2O absorption chillers recently, due to its relatively simple configuration and low requirements on heat sources [28–33]. Furthermore, the COP of double-effect LiBr-H_2O absorption chiller systems is almost twice higher than those of with single-effect systems. With double-effect systems, it is possible to obtain a coefficient of performance as high as 1.12 at a condenser temperature of 30 °C. Nonetheless, they need a generator temperature higher than 140 °C to reach an evaporator temperature as low as −5 °C [34–38]. Besides, there are some high requirements that heat sources should be more than 120 °C. Given this, the construction of double-effect LiBr-H_2O system is sophisticated, which needs high investment and operation cost. Nevertheless, the CO_2 emission of the single-effect system is respectively about 1.9 and 1.7 times higher than direct-fired and hot-water double-effect system, according to the report of Avanessian and Ameri [39].

The efficiency enhancement of the solar absorption cooling system components is essential to increasing the COP of the whole system [40, 41]. A performance evaluation of a 35 kW LiBr-H_2O absorption machine driven by 72 m^2 heat pipe evacuated tube collector with a gas backup system was made. The results show that the actual average COP of the system was 0.33, while the maximum and minimum values were 0.50 and 0.17, respectively. These results were obtained based on the average collector efficiency and the solar fraction of 0.55 at an ambient temperature of 32 °C [42]. Lu et al. [43] investigated one two-phase thermo-syphon silica gel-water solar adsorption chiller and LiBr-H_{dd} absorption chiller with the new media compound parabolic concentrator (CPC) solar collectors. The results reveal that the efficiency of the medium temperature evacuated-tube CPC solar collector could reach 0.5, when the hot water temperature was 125 °C. The average solar COP of absorption system was 0.19. Ali et al. [44] investigated the performance of an integrated free cooling and solar powered single-effect LiBr-H_2O absorption chiller in Oberhausen (Germany). The plant included a 35.17 kW cooling absorption chiller, 108 m^2 evacuated tube collectors, a 6.8 m^3 hot water tank, a 1.5 m^3 cold water tank, and a 134 kW cooling tower. The results illustrate that the chiller efficiency could reach 70% in some cooling months, while it was about 25% in the 5 years of plant operation; the monthly average efficiency value of collectors varied from 34.1% to 41.8%, and the average value of the 5 years was about 28.3%. Hang et al. [45] made an analysis on the energy performance of a solar absorption cooling system, a 23 kW double-effect absorption chiller driven by a 54 m^2 external compound parabolic concentrator (XCPC) solar collectors. The results suggest that the daily average collector efficiency changed between 36% and 39%. The average coefficient of performance (COP) of the LiBr absorption chiller was between 0.91 and 1.02, with an average value of 1.0. The daily solar COP was approximately 0.374. This demonstrates that this chiller should be operated under the condition that the temperature of the hot water supplied to the generator is 85 °C, to obtain a high COP for a small-size absorption chiller developed from an old out-of-order commercial chiller [46]. Therefore, Calise et al. [47] simulated different solar cooling systems to find out the appropriate operation parameters for maximizing the COP of solar cooling systems.

Solar Adsorption Cooling System

Working Principle of Solar Adsorption Cooling System

Adsorption cooling can be achieved through the cycle of adsorption/desorption of liquid refrigerant on the solid adsorbent driven by the thermal energy collected in the adsorbent bed from solar energy. The working principle of solar adsorption cooling system is shown in Fig. 2.

When the adsorption bed is arranged outside, the solid adsorption in the bed is heated by the solar energy during daytime. In this period, the low boiling point liquid refrigerant adsorbed on the solid adsorbent is gradually heated and vaporized into a gaseous state. At this moment, the gaseous refrigerant overflows from the solid adsorbent. After being cooled in the condenser, it then flows into the accumulator. In the cooling process, the

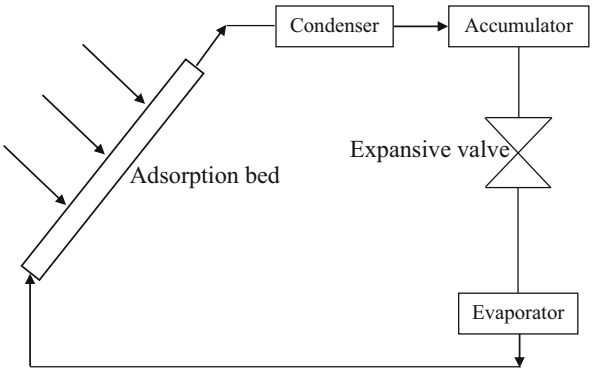

Fig. 2 Working principle of solar adsorption cooling

liquid refrigerant flows through the expansive valve, get throttled into the low-temperature and low-pressure liquid refrigerant, and then inflows into the evaporator to absorb heat. When the heating process of the adsorption bed stops, the temperature and pressure in the adsorption bed decrease. Hence, under the driving force from the bed pressure and the adsorption capacity of solid adsorbent, the endothermic refrigerant in the evaporator flows into the adsorbent bed and gets adsorbed by the solid adsorbent. At this time, a complete cooling cycle is ended. The common adsorption cooling pairs are active carbon–methanol, molecular sieve–water, silica–water, active carbon–ammonia, calcium chloride–ammonia, and metal hydride–hydrogen. Single-bed and multi-bed adsorption heating are two main adsorption heating modes.

Solar adsorption cooling has become not only an important branch of energy saving technology but also a major research topic. Compared with other cooling systems, solar adsorption cooling system has the following characteristics:

1. The structure of the system is simple, and its operation is easy. It requires no solution pump or rectifying devices. Therefore, the running cost of this system is low. There is also no refrigerant contamination, crystallization, or corrosion problem. For a basic adsorption ice-making cycle driven by solar energy, there is no moving part or power consumption.
2. Different adsorption working pairs can be chosen for distinct heating and evaporation temperatures. For instance, a solar adsorption air-conditioning system with a silica gel-water working pair can be driven by the hot water of 65–85 °C for producing the chilling water at 7–20 °C. A solar adsorption ice maker with activated-methanol working pair can be directly driven by the solar radiation on the solar collectors.
3. The requirement of air-conditioning on the cooling power of the system can match solar radiation. The stronger the solar radiation is, the hotter the weather is, the greater the required cooling load is, and consequently the larger the cooling power of the system is.
4. Compared with the absorption and compression cooling systems, the adsorption system has a relatively small cooling power. Because of the critical heat and mass transfer performance, the mass of the adsorbent and heat exchanger will increase

as the cooling capacity increases. Consequently, the initial investment will rise as well, and the machine will be large. In addition, due to the low energy density of solar radiation on the ground, a relatively large collector area for collecting a certain amount of heating power is required. For the reasons above, it is difficult to develop successful solar ice makers, refrigerators, or air conditioners.

5. As solar energy depends on seasons, it is provided periodically and intermittently. The solar-driven adsorption cooling system usually needs an auxiliary thermal source, when it is applied as an air-conditioning or cold storage system.

The main feature of an integrated solar adsorption cooling system is the use of adsorption collector, which is a combination of an adsorbent bed and a solar collector. During day time, it absorbs solar energy and desorbs it. At night, it produces cooling capacity through adsorption. The adsorption cooling cycle is the basic intermittent cycle.

Mathematical Models of Solar Adsorption Cooling System

Solar Collector Performance

The performance of the solar collector can be estimated based on collector efficiency and collector temperature. Collector efficiency (η) is the ratio of the heat energy (Q_{seff}) transformed from the actual solar radiation (Q_{solar}).

Collector efficiency:

$$\eta = \frac{Q_{seff}}{Q_{solar}} \tag{1}$$

Effective heating power:

$$Q_{seff} = \int_{T_1}^{T_2} \left(M_a\left(C_{pa} + xC_{pr}\right) + M_m C_{pm}\right) dT + L_{ref}\,\Delta x M_a \tag{2}$$

Solar radiation:

$$Q_{solar} = \int_0^t I(t) A_{seff}\, dt \tag{3}$$

Wherein, M_a is the mass of adsorbent, C_{pa} the specific heat of adsorbent, and C_{pr} the specific heat of the refrigerant. x denotes the adsorption quantity, and $M_m C_{pm}$ the heat capacity of the entire adsorption collector, except for the adsorbent and refrigerant. L_{ref} signifies the latent heat of refrigerant, I the solar radiation intensity, A_{seff} the effective collector area, and t the duration time of sunshine.

Cooling Performance

The cooling performance of a solar adsorption cooling system can be indicated by the coefficient of performance (COP). Usually, there are two coefficients. One is the

coefficient of the cooling performance of adsorption system. It can be expressed as the ratio of the cooling capacity to the effective heating power provided by the adsorption collector:

$$COP_{ref} = \frac{Q_{ref}}{Q_{seff}} \tag{4}$$

Wherein, Q_{ref} is the cooling capacity. It can be calculated by $Q_{ref} = Q_{eref}Q_{cc}$. Q_{eref} is the evaporation cooling capacity in the evaporator, which can be calculated by the following equation:

$$Q_{ref} = \Delta x M_a L_{ref} \tag{5}$$

Wherein, $^{\triangle}xM_a$ represents the desorption mass of the refrigerant in the heating process of the adsorbent. It is also the cycle amount of the refrigerant in one cycle.

Q_{cc} indicates the sensible heat released by the refrigerant in the cooling process from the condensing temperature to the evaporation temperature.

$$Q_{cc} = \int_{\mathrm{Te}}^{\mathrm{T_c}} M_a \Delta x C_{pr} dT \tag{6}$$

Another important coefficient is the coefficient of solar cooling performance. It can be expressed as the ratio of the cooling capacity to the total solar radiation received by the adsorption collector:

$$COP = \frac{Q_{ref}}{Q_{solar}} \tag{7}$$

Structure of Solar Adsorption Cooling System

Since the desorption temperature of the activated carbon-methanol working pair is low (70–100 °C), it is an ideal working pair for a solar adsorption cooling system. The characteristic of this kind of system lies in that the adsorber is a finned-tube adsorption bed/collector [1]. The structure of a novel solar powered finned-tube solar adsorption ice-making machine is displayed in Fig. 3. The adsorption cooling system consists of three parts, namely the adsorber, the condenser, and the evaporator.

For achieving a high-performance adsorption bed collector, there are some basic optimization directions for the adsorption bed structure. The first one is to expedite the pass of the heat absorbed by the adsorbent bed to the adsorbent for desorbing the adsorbate by improving the heat transfer structure of the adsorbent bed. The second is to enlarge the mass transfer channels in the adsorbent bed to facilitate the desorbed adsorbate to get into the condenser as soon as possible, and thereby maintain the pressure steady in the adsorption bed, which is favorable to the desorption of more adsorbate. The third is to use the adsorption bed material with a low heat capacity to reduce the energy consumption of the adsorption bed. The last is to improve the thermal insulation of the adsorption bed to decrease heat loss.

Fig. 3 Solar-powered adsorption ice-making machine

Based on the above considerations, the key component of the adsorption bed collector, i.e., an enhanced heat and mass transfer finned-tube casing, was designed. As shown in Fig. 4, the outer tube of the metal casing absorbed the solar radiation. The inside of the inner tube served as the mass transfer channel. The space between the inner tube and the outer tube was filled with the adsorbent, i.e., activated carbon. The inner tube was intermittent, and the discontinuous parts of the inner tube were attached to a fine metal mesh, which prevented the adsorbent from entering into the mass transfer channel. Meanwhile, the desorbed adsorbate could get inside the inner tube through the mesh and flow into the condenser. The fins connected the inside tube and the outside tube, reinforced the strength of the casing, and enhanced the heat transfer in the adsorption bed. Compared with the metal casing with the same inner and outside diameters, the finned-tube casing had a heat transfer area per unit length of more than 51.4%. The six wide slits in the inner tube could increase the mass transfer area between the adsorbent and the center channel by 30.7%, compared with the perforation in the inner tube (with a gape diameter of 0.45 mm and a perforation interval of 1.45 mm). Aluminum alloy was utilized to build the casing due to its high thermal conductivity, low specific heat capacity, and low cost.

As shown in Fig. 5, the adsorption bed collector was composed by a glass cover, a frame structure, thermal insulation materials, and finned-tube casings. The sunshine

Fig. 4 Configuration of the finned-tube adsorption casing

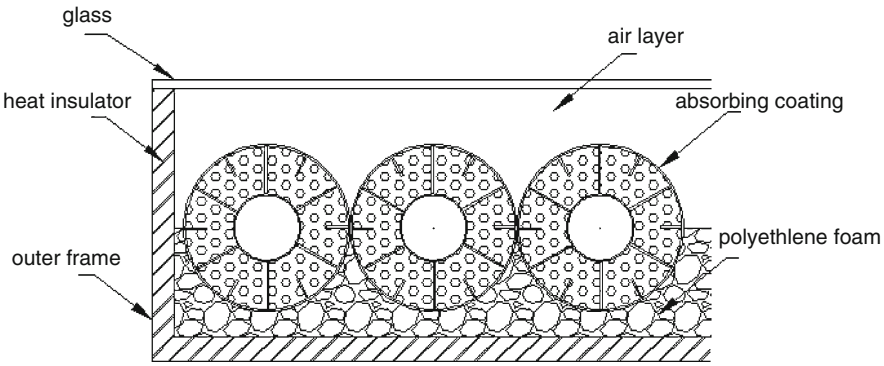

Fig. 5 Cross-section diagram of the adsorption bed collector

side of the finned-tube casings was sprayed with solar selective absorbing coatings. The space in the backlight side of the finned-tube casings and the bottom of the frame were filled with polyethylene foam to reduce heat loss. The adsorption casings were closely arranged in the frame for effectively utilizing the collector area and increasing the filling amount of adsorbent. The finned-tube casings were placed horizontally, and divided into the upper group and the lower group. Each group had six finned-tube casings. Both ends of the finned-tube casings were connected to a confluence pipe with a diameter of 25 mm. The adsorption bed collector was installed with an inclination of 15°, and its surface faced south.

Ice Production and Coefficients of Performance

According to the adsorption cooling mechanism, the adsorbate was desorbed out in the process of rising adsorption bed temperature and adsorbed in the process of reducing adsorption bed temperature. Meanwhile, the adsorption heat was released to relieve the temperature drop in the adsorption bed. In the whole cycle process, the

Table 1 System cooling performance under typical weather conditions

	Condition 1	Condition 2	Condition 3	Condition 4
Ice/cold water mass (kg)	6.5/1.5	4.6/3.4	1.8/4.2	0/6
The total radiation (MJ)	20.460	21.479	15.586	11.51
Direct cooling capacity (MJ)	2.490	1.991	1.287	0.418
Dissipative cooling capacity (MJ)	0.0216	0.031	0.059	0.036
COP_{solar}	0.122	0.094	0.086	0.039
Weather conditions	Sunny, clear sky	Sunny, partly cloudy sky	Cloudy	Overcast sky

Fig. 6 Ice-making results

adsorbent bed experienced a maximum temperature. Then, the adsorbent bed temperature began to decline, although the adsorption bed collector still received solar radiation at that time. The part of solar radiation energy was not utilized for desorbing the adsorbate, and it was wasted.

Table 1 shows the system cooling performances of the solar-powered adsorption cooling system with valve control in adsorption/desorption process under four typical weather conditions, namely sunny and clear sky, sunny and partly cloudy sky, cloudy sky, and overcast sky. The close time of the valve was within half an hour after the adsorption bed temperature reached the maximum. The COP was 0.122, 0.094, 0.086, and 0.039, respectively, on 4 different days. Ice-making phenomena under these four weather conditions were observed in Fig. 6.

Figure 7 presents the temperature changes in the evaporator at the adsorption stage under four typical weather conditions (adsorption/desorption process with valve control). From Fig. 7, it can be seen that the adsorption cooling rate was faster under the condition of sunny and clear sky. The time consumed was around 3 h from the start point of the temperature drop to the lowest point. It was around 5 h under the condition of sunny and partly cloudy sky as well as cloudy sky. Under the condition of overcast sky, the time consumed was more than 6 h. Thus, it is a feasible way to

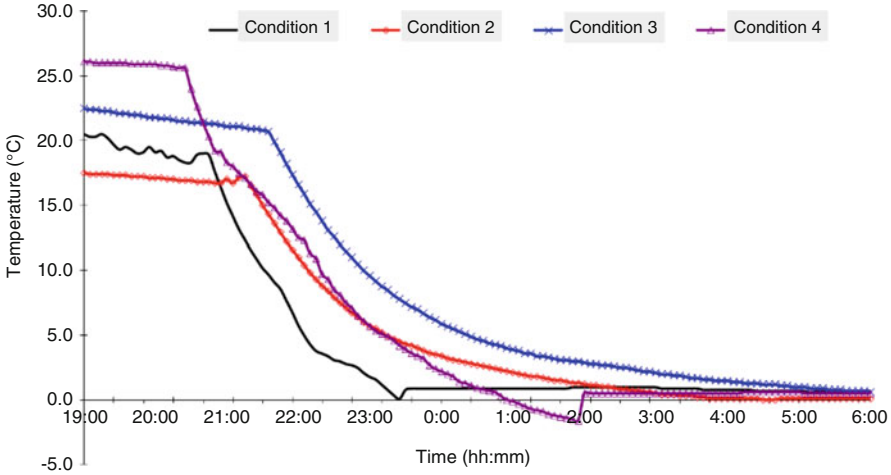

Fig. 7 Temperature changes with time in the evaporator under four typical weather conditions

apply the activated carbon particles with large diameters to decrease the adsorption time consumed.

Solar Absorption Cooling System

Working Principle of Solar Adsorption Cooling System

Solar absorption cooling uses solar energy as the driving source to make relative changes in the concentrations of two kinds of liquid solutions: refrigerants and absorbents. The working principle of solar adsorption cooling system is exhibited in Fig. 8.

Solar absorption cooling system is mainly composed of solar collector, hot water storage tank, absorption chiller, and cooling tower. The absorption chiller is made up of generator, condenser, expansion valve, evaporator, and absorber. The absorption cooling cycle has five processes, including generation process, condensation process, throttling process, evaporation process, and absorption process.

On sunny days, the water stored in the tank is heated by the solar irradiance in the solar collector. The hot water is pumped into the generator of the absorption chiller to heat the absorbent solution. In the generator, the generator pump sends the absorbent solution into the generator, and the solution is heated by the hot water produced by the collector. Then, the water in the generator absorbs heat and vaporizes into water vapor. The vapor is the high-temperature and high-pressure gaseous refrigerant, and the aqueous content of the adsorbent solution rises continuously. The continuously precipitated water steam enters into the condenser. After being cooled by the cooling water from the cooling tower, the steam is condensed into liquid water. Subsequently, the fluid refrigerant flows into the U-shape throttling device. The U tube acts as a liquid seal tool to prevent the steam from entering directly into the evaporator. Then,

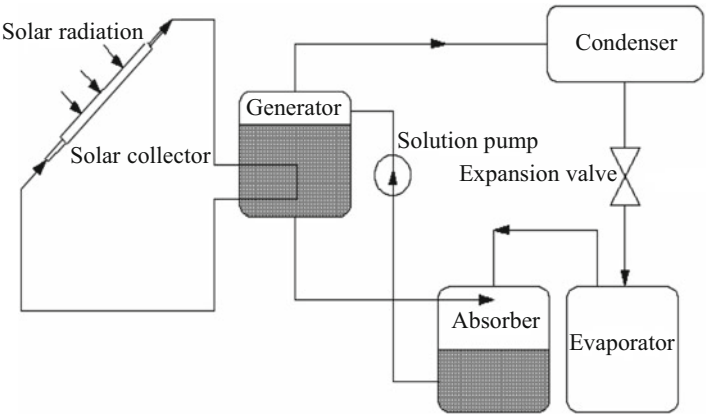

Fig. 8 Working principle of solar absorption cooling system

the liquid refrigerant is pushed into the evaporator. When the liquid refrigerant inflows into the evaporator, the pressure of the liquid water drops sharply, while part water vapor is flushed out and most water is sprayed out by the injector onto the outface of the cooled water pipes. Then, the vapor turns into low-pressure water vapor after absorbing the heat of the cooled water flowing in the pipes. The concentrated absorbent solution flows into the absorber and mixes with the dilute solution in the absorber to form a solution with an intermediate concentration. In the absorber, the water vapor that flows out of the evaporator is absorbed by the absorbent solution.

Structure of Solar Adsorption Cooling System

Solar adsorption cooling system is made up of solar collector and adsorption refrigerator. Solar collector mainly consists of vacuum tube collector, plate collector, and parabolic trough solar collector (PTC). Adsorption refrigerator comprises single-effect adsorption refrigerator, double-effect adsorption refrigerator, and multieffect absorption chiller. In this chapter, a 23 kW single-effect lithium bromide absorption chiller (TX-23) driven by the parabolic trough solar collector (PTC) is analyzed.

Figure 9 gives the schematic diagram for the main parts of the experimental cooling system, including PTC array, hot water storage tank (with a supplemental water tank), single-effect lithium bromide absorption chiller (TX-23), cooling tower, and blower coils installed in the meeting room. Figure 9 also illustrates the positions of temperature test points. Table 2 and Fig. 9 display the temperatures of sensors and instruction.

Figure 10 presents the main parts of the cooling experimental system. The main measurement and instrument accuracies of the monitoring system are shown in Table 3.

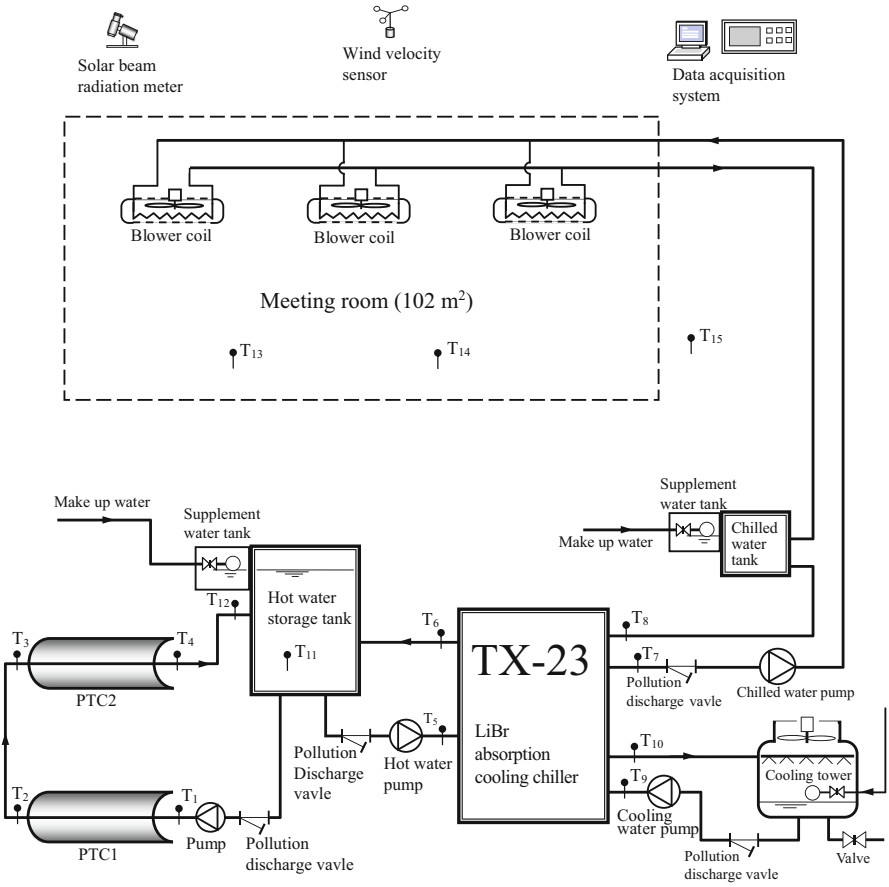

Fig. 9 Scheme diagram of solar-powered absorption cooling system

The parameters and heat efficiency values at different temperatures of PTC array are listed in Table 3. The heat receiver, i.e., glass-metal evacuated absorber tube, is the core component of PTC, and the specifications are also shown in Table 4. The PTC array is made up of two PTCs in series, and the array space between two PTCs is 5.6 m. Table 5 gives some parameters of the cooling chiller. The capacity of hot water storage tank is 1 m^3. Table 6 lists the cooling tower parameters. The same type of cooling water is used in the cooling tower. The area of end air-conditioning room is 102 m^2, and three blower coils are installed on the top of the meeting room. (Relevant parameters are shown in Table 7.) The room is utilized as conference room, which can accommodate more than 20 people. The height of the room is 3.5 m. The length and the width are 13.6 m and 7.5 m, respectively. There are two windows with 10 m^2 of transparent fiberglass in the north wall. The south wall nearby the corridor has two glass doors, and the area of each door is 3 m^2.

Table 2 Instructions for the temperature probes

Temperature probe	Measurement explain
T_1	Inlet temperature of PTC1
T_2	Outlet temperature of PTC1
T_3	Inlet temperature of PTC2
T_4	Outlet temperature of PTC2
T_5	Hot water inlet temperature of chiller
T_6	Hot water outlet temperature of chiller
T_7	Chilled water inlet temperature of chiller
T_8	Chilled water outlet temperature of chiller
T_9	Cooling water inlet temperature of chiller
T_{10}	Cooling water outlet temperature of chiller
T_{11}	Outlet temperature of hot water tank
T_{12}	Inlet temperature of hot water tank
T_{13}, T_{14}	The indoor temperature of meeting room
T_{15}	The outdoor temperature of meeting room

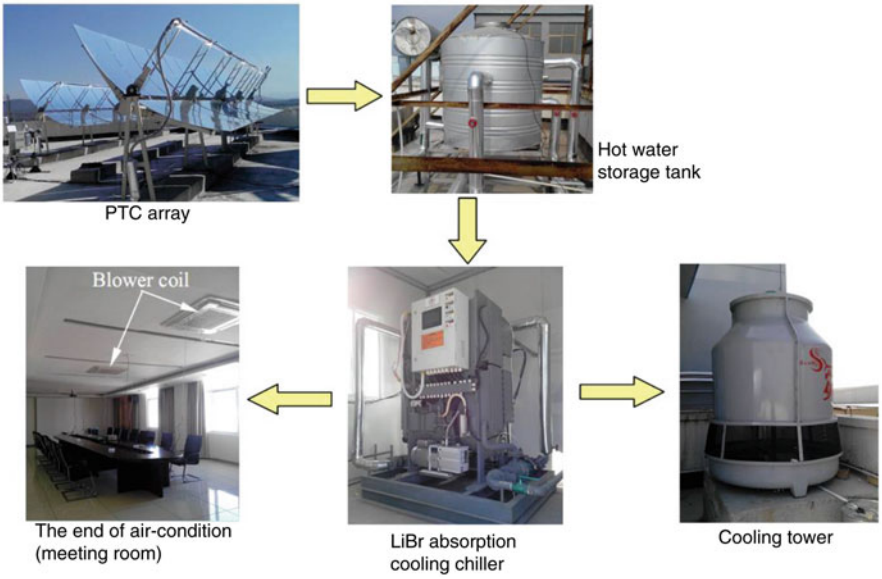

Fig. 10 Main parts of solar absorption cooling system

Then, the last two walls are made up of reinforced concretes with a thickness of 10 cm.

Energy Conversion Analysis of the Solar Adsorption Cooling System

The heat flow diagram of the absorption chiller is shown in Fig. 11.

The main energy conversion processes of solar adsorption cooling are as follows:

Table 3 Main measurement and instrument accuracies of the monitoring system

Instrument	Model	Range	Accuracy	Application scope	Maximum relative error	Maximum absolute error	Uncertainty (B class)
Pyranometer	Kipp & Zonen CMP-6	0–2000 (W/m^2)	±5%	0–1000 (W/m^2)	±10%	±100 W/m^2	57.7348 W/m^2
Thermocouples	T	−200 to 350 (°C)	±0.4%	0–150 (°C)	±0.93%	±1.4 °C	0.8083 °C
Wind speed transducer	EC-9S	0–70 (m/s)	±0.4%	0–10 (m/s)	±2.8%	±0.28 m/s	0.1617 m/s
Electromagnetic flow meter	KROHNE OPTIFLUX 5300	DN 25; 0–12 (m/s)	±0.15%	0–5 (m/s)	±0.36%	±0.018 m/s	0.0104 m/s
Pressure transducer	YOKOGAWA EJA430E	0.14–16 (MPa)	±0.055%	0–2 (MPa)	±0.44%	±0.0088 MPa	0.0051 MPa

Table 4 PTC array parameters

Parameter	Value
Aperture area	56 m^2
Aperture width	2.5 m
Orientation	North-south ($\psi = 0°$)
Length of PTC	26 m
Focal distance of parabolic trough	1.1 m
The width of focal spot	5 m
PTC efficiency values at different temperature	77.5% (30 °C), 68.4% (50 °C), 57.3% (70 °C), 38.4% (90 °C)
Inner diameter of metal pipe of receiver	4 cm
Outer diameter of glass pipe of receiver	11 cm

Table 5 PTC array parameters

Parameter	Value
Model	TX-23
Working pair	Lithium bromide-water
Ambient temperature	28–36.0 °C
Hot water temperature at chiller inlet	50–90.0 °C
Hot water temperature at chiller outlet	49–80.0 °C
Outlet temperature of chilled water	10.0–14.0 °C
Inlet temperature of chilled water	15.0–22.0 °C
Cooling water temperature at chiller inlet	20.7–27.8 °C
Cooling water temperature at chiller outlet	23.5–29.3 °C
Power dissipation	2.3 kW
Cooling capacity	23 kW
Chilled water rate	4.0 m^3/h
Hot water rate	5.7 m^3/h

Table 6 Parameters of cooling tower, tank, and pumps

Parameter	Value
Model	BLT-10
Wind rate	10.5 m^3/h
Cooling water rate	10 m^3/h
Dynamo power	0.75 kW
Capacity of tank	1 m^3
Insulation thickness of tank	3 cm
Pump of PTC	0.33 kW
Hot water pump	0.78 kW
Chilled water pump	0.78 kW
Cooling water pump	0.98 kW

Table 7 Parameters of blower coil

Parameter	Value
Model	EKCW800KT
Wind rate	1360 m^3/h
Cooling power	7200 W
Input power	130 W

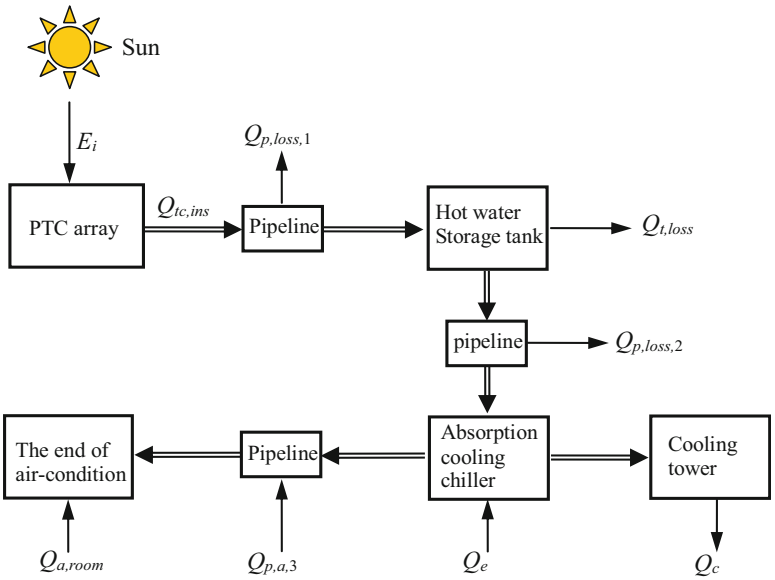

Fig. 11 Main parts of solar absorption cooling system

1. The input of solar radiation into PTC:

$$E_i = I_b A_c \cos\theta \tag{8}$$

Wherein, I_b, A_c, and θ are the solar beam radiation, the collection area, and the incident angle of sun ray, respectively.

2. The transformation of useful energy from the received solar radiation $Q_{tc.ins}$ as shown as:

$$Q_{tc,ins} = m_F c_p[(T_2 - T_1) + (T_4 - T_3)] \tag{9}$$

Wherein, m_F is the mass flow rate of the water flowing in the receiver of PTC array, and C_p is the specific heat capacity under constant pressure.

3. The pipeline heat loss between PTC and hot water storage tank $Q_{p,loss,1}$:

$$Q_{p,loss,1} = m_F c_p[(T_{11} - T_1) + (T_2 - T_3) + (T_4 - T_{12})] \tag{10}$$

4. The calculation of the heat loss of hot water storage tank $Q_{t,loss}$ is relatively complicated. The heat loss of hot water tank was tested in accordance with ISO 9459 and EN12976. Before the experiment, the water in the tank was heated by PTC, and the temperature was not lower than 60 °C. In order to ensure the consistency of temperature in the tank and avoid thermal stratification in the tank, an external water loop was adopted. The water was pumped out of the tank in the bottom and back into the tank in the top by the hot water pump. Then, the hot water was circulated through the external water pump. The pump and the circulation pipes were wrapped with insulation materials, with a thickness of no less than 3 cm. Three temperature sensors were arranged at equal intervals in the vertical direction inside the hot water tank. When the values of sensors were close, there was no thermal stratification in the tank. Then, the circulation pump must be shut down. The hot water temperature was 63.6 °C. The water was placed for 15 h without any interference. Subsequently, the circulation pump was turned on once again, and the hot water was circulated until the temperatures of sensors became nearly the same. The temperature was 49.8 °C. In real experimental test, we could use the simple formula below to calculate it:

$$P_{t,loss,av} = \frac{m_{w,t} c_p \Delta T}{\Delta t} \tag{11}$$

Wherein, $m_{w,t}$ denotes the water mass in the tank, Δt the duration of experiment, and ΔT is the temperature difference of water with no thermal stratification in the tank within Δt. When $\Delta t \to 0$, the instantaneous heat power loss could be gained.

5. The pipeline heat loss between hot water storage tank and chiller:

$$Q_{p,loss,2} \approx 2m_{F,g} c_p (T_{11} - T_5) \tag{12}$$

Wherein, $m_{F,g}$ signifies the mass flow rate of the water flow passing by the generator of the chiller.

6. The heat absorbed from the chilled water in the evaporator of cooling chiller is expressed with $Q_{p,loss,2}$. (This issue will be analyzed in the next section.)
7. The heat output from absorber and condenser to cooling water can be equivalent to the output heat Q_c from cooling tower.
8. $Q_{p,a,3}$ is the heat absorbed from the pipeline between the chiller and the meeting room, which comes from the outer surface of the pipeline.

9. $Q_{a,room}$ is the heat absorbed from the blower coils, which comes from the air in the meeting room.

Thermal Efficiency of the Heat Collection System

Thermal Efficiency of the PTC Array

The functions of instantaneous thermal power and instantaneous thermal efficiency are as follows:

$$P_{te,ins} = m_F c_p[(T_2 - T_1) + (T_4 - T_3)] \tag{13}$$

$$\eta_{te,ins} = \frac{P_{te,ins}}{I_b A_c \cos\theta} \tag{14}$$

The roof orientation factor the PTC array could be shaded by adjacent buildings after 4:30. Therefore, the experiments could only be conducted before 4:30. Besides, they were made under the condition of windy weather. The tested peak wind velocity reached 8 m s^{-1}, which was largely influential to the thermal efficiency of PTC array, because the focal line was frequently moved out of the absorber tube under such condition.

Figure 12 gives the test results of the thermal efficiency of PTC array. Obviously, when the irradiance changed from 0.80 kW m^{-2} to 0.90 kW m^{-2}, the instantaneous thermal efficiency ranged from 0.50 to 0.65. At the same time, the instantaneous thermal power of the system was changed between 24 kW and 27 kW. The mass flow rate of water m_F was calculated to be 0.602 kg s^{-1}.

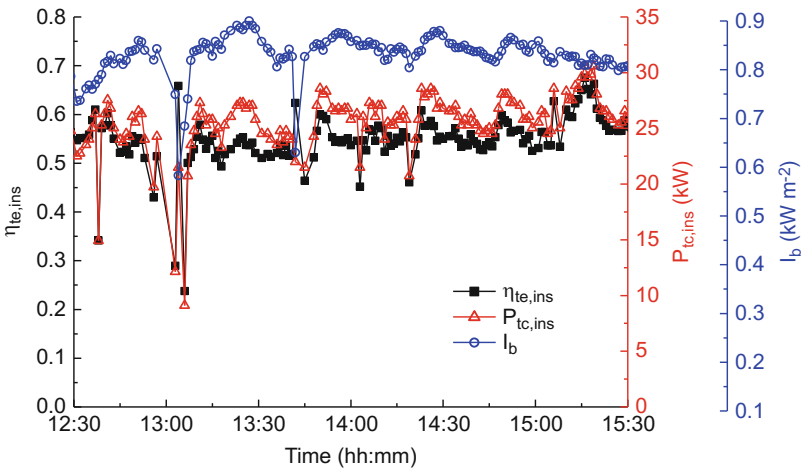

Fig. 12 Test results of the instantaneous efficiency and power of PTC array

Table 8 Parameters of pipes and their energy losses

Pipeline type	Inner tube diameter (cm)	Outer tube diameter (cm)	Insulation thickness (cm)	Pipe length (m)	Total energy losses (kW)	Note
Pipeline between PTC	4	12.5	4	78	3.90–6.20	60–90 °C (heat loss)
And hot water storage tank pipeline between hot water storage tank and chiller	4	12.5	4	18	0.90–1.40	60–90 °C (heat loss)
Pipeline between chiller and blower coil	4	10	3	55	0.27–0.55	7–16 °C (cooling loss)

Energy Losses from the Pipelines

In this research, the tests on the energy losses of the pipeline sections between the PTC and the hot water storage tank, between the hot water storage tank and the chiller, as well as between the chiller and the meeting room were conducted.

The heat conduction coefficient of the thermal insulation layer of pipeline was between 0.037 W m^{-1} K^{-1} and 0.040 W m^{-1} K^{-1}. The outer surface of the thermal insulation was wrapped with aluminum alloy layer. The heat losses of the three types of pipelines are shown in Table 8.

It is worth pointing out that heat was absorbed from the outside of their tubes, because the temperature of the chilled water inside the tube was lower than that of the outside. Therefore, the energy losses of the pipeline between the chiller and the meeting room were cooling losses, rather than heat losses.

The heat loss of water storage tank was tested as well. At first, the tank was filled with 688 kg of hot water. Fifteen hours later, the temperature of water was decreased from 63.6 °C to 49.8 °C. It can be estimated that the average heat power loss was about 640 W. Obviously, the average heat power loss increased with the increase of hot water temperature.

Taking the heat losses of pipeline and heat losses of hot water tank into consideration, the instantaneous power of the heat collection system can be expressed as follows:

$$P_{tc,ins,s} = P_{tc,ins} - P_{p,loss} - P_{t,loss} \tag{15}$$

The instantaneous thermal efficiency of the heat collection system can be expressed as follows:

$$\eta_{te,ins,s} = \frac{P_{tc,ins} - P_{p,loss} - P_{t,loss}}{I_b A_c \cos\theta} \tag{16}$$

Wherein, $P_{p,loss}$ and $P_{t,loss}$ are the heat losses of the pipelines and the hot water tank, respectively. Thus, when the solar beam radiation changed between

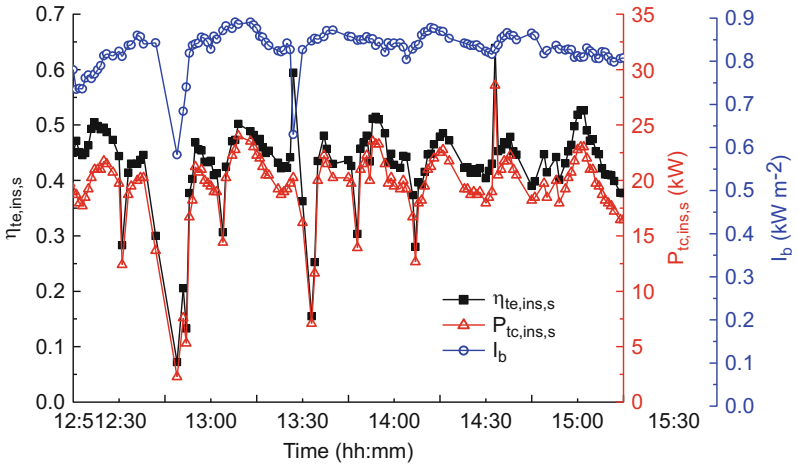

Fig. 13 Thermal efficiency and power of heat collection system

0.80 kW m^{-2} and 0.90 kW m^{-2}, the instantaneous thermal efficiency and power ranged from 0.32 to 0.42 and from 17 kW to 21 kW, respectively, as shown in Fig. 13.

Performance of the Cooling System

The experiment was conducted mainly to test and investigate the performance of the cooling system. During the experiment, many parameters, such as solar beam radiation, wind velocity, ambient temperature, inlet and outlet temperature of PTC, hot water storage tank, heating, chilled water, and cooling water, were tested.

Energy Analysis of the Cooling Process for the Cooling Chiller

Thermodynamic coefficient (η_r) was considered as the economy evaluation, which was expressed as follows:

$$\eta_r = P_e / P_g \tag{17}$$

Wherein, P_e is the absorption power from the chilled water vapor, and P_g is the consumption amount of heat energy.

The consumed thermal power of the generator is as follows:

$$P_g = m_{F,g} c_p (T_6 - T_5) \tag{18}$$

The absorption power from the chilled water of water vapor is as follows:

$$P_e = m_{F,e} c_p (T_7 - T_8) \tag{19}$$

The function of the power output into the cooling water by the absorber and the condenser is as follows:

$$P_c = m_{F,c} c_p (T_{10} - T_9) \tag{20}$$

In the three equations above, $m_{F,g}$, $m_{F,c}$, and $m_{F,e}$ are the mass flow rates of hot water, chilled water, and cooling water, respectively. T_5–T_{10} indicate the inlet and outlet temperatures of hot water, chilled water, and cooling water.

According to the analysis above, if ignored the power consumed by circulating the water pump, the cycle cooling coefficient of the chiller (the chiller efficiency or the COP of the chiller) can be expressed as follows:

$$\eta_r = \frac{P_e}{P_g} = \frac{m_{F,e} c_p (T_7 - T_8)}{m_{F,g} c_p (T_6 - T_5)} = \frac{m_{F,e} (T_7 - T_8)}{m_{F,g} (T_6 - T_5)} \tag{21}$$

Performance Analysis of the Absorption Cooling System

A 10-day experiment on the cooling performance of the absorption chiller was conducted. It lasted from April to May 2014. At first, the water in the tank must be heated by PTC. When the temperature of hot water in the tank reached more than 65 °C, the cooling chiller was turned on manually. In order to understand the performance of the chiller under different operating temperatures, diverse water temperatures were adopted to drive the chiller. The cooling performance was obtained and recorded. Nonetheless, in order to protect the cooling chiller, the test experiment must be terminated when the hot water temperature in the tank descended to around 40 °C. All the components were controlled manually. During the experiment, the test values of m_F, $m_{F,g}$, and $m_{F,c}$ were 0.602 kg s^{-1}, 1.36 kg s^{-1}, and 0.90 kg s^{-1}, respectively.

The experimental results are listed in Table 9. Figures 14, 15, 16, and 17 exhibit the changing curves of system performance parameters with time. The figures show

Table 9 Average COP of the cooling system

Date (2014)	Weather condition	$E_{i,tot}$ (MJ)	Q_r (MJ)	$\eta_{r,av}$	$COP_{s,av}$
April 4	Cloudy and windy	448	54	0.18	0.12
May 10	Cloudy and windy	643	84	0.21	0.13
May 11	Cloudy and windy	549	58	0.17	0.11
May 13	Sunny and windy	1300	220	0.51	0.17
May 14	Sunny and windy	1200	170	0.45	0.14
May 15	Sunny and windy	1122	234	0.57	0.21
May 16	Sunny and windy	1120	267	0.58	0.23
May 17	Sunny and windy	1280	284	0.51	0.22
May 18	Sunny and windy	1262	313	0.55	0.25
May 19	Sunny and windy	877	288	0.59	0.23
May 20	Cloudy and windy	690	158	0.51	0.21
May 21	Sunny and windy	967	270	0.57	0.27
May 22	Sunny and windy	1110	262	0.47	0.24
May 24	Sunny and windy	1084	234	0.50	0.22

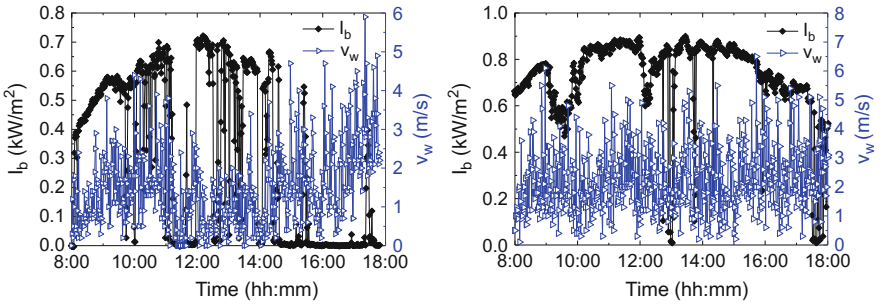

Fig. 14 Solar beam radiation and wind velocity vs. time

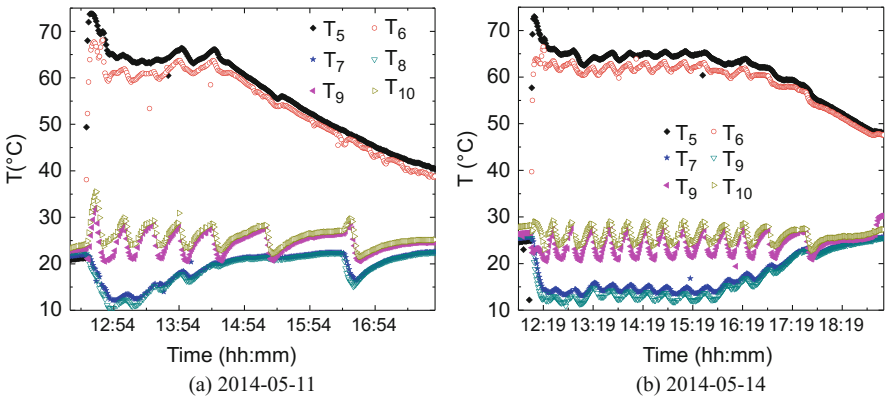

Fig. 15 Inlet and outlet temperatures of the heating, chilled, and cooling water of the chiller vs. time

the experimental results in 2 days. Table 9 gives the experimental results of cooling performance during those 14 days.

According to Fig. 14, the wind speed was high on most of sunny and cloudy days during the experiment, and the maximum wind velocity v_w reached 8 m s^{-1} (It generally ranged from 2 m s^{-1} to 5 m s^{-1}.), which had a huge impact on the thermal efficiency of PTC system.

In accordance to Fig. 15, when the operating temperature of the cooling chiller (the temperature of hot water) increased from 39 °C to 80 °C, the lowest temperature of chilled water could reach 9 °C. At the same time, the temperature of cooling water changed between 20 °C and 35 °C. The cooling process was disconnected. At the beginning of the experiment, the temperatures of hot water and chilled water decreased rapidly. As the chiller operated steadily, the system performance parameters changed stably with time. The higher the inlet temperature of hot water was, the lower the outlet temperature of chilled water was.

Figure 16 presents the changing curves of the cooling coefficient and power of the chiller with time. As can be seen, the cooling coefficient η_r increased along with the increase in the cooling quantity P_r of the chiller.

As shown in Fig. 17, the indoor temperature of the meeting room decreased sharply in the first 30 min after the operation of the cooling chiller. After reaching a certain value, the indoor temperature began to stabilize gradually. Sometimes the temperature fluctuated slightly. The indoor temperature increased along with the ambient temperature.

Table 9 displays the average performance coefficient of the cooling system on each experimental day. Wherein, $E_{i,tot}$ indicates the total incident solar radiation energy (the total solar radiation energy input into PTC), and Q_r the total cooling quantity. $\eta_{r,av}$ represents the average cooling efficiency, and $COP_{s,av}$ the average COP of the cooling system. The total incident solar radiation energy $E_{i,tot}$ is expressed as follows:

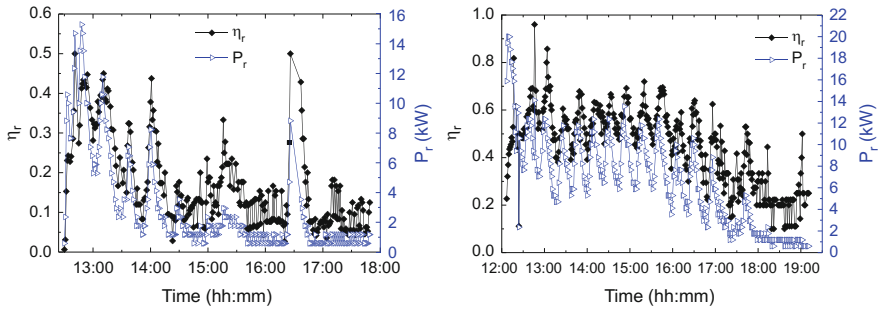

Fig. 16 Cooling coefficient and power of the absorption cooling chiller

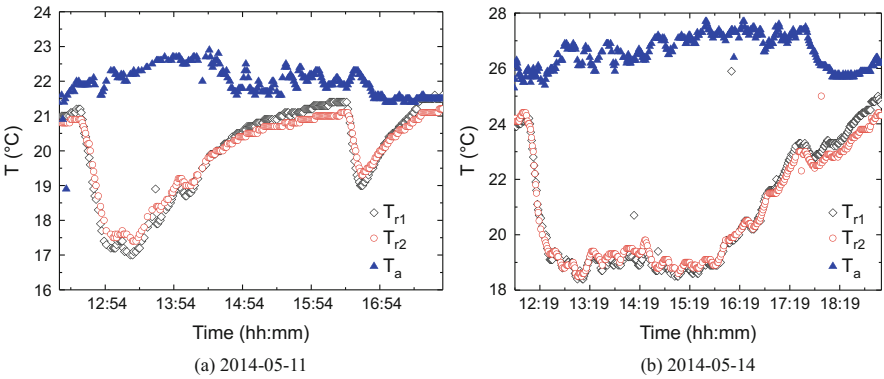

Fig. 17 Variation of indoor temperatures in the cooling process

$$E_{i,tot} = \int_{t_{s,bt}}^{t_{s,st}} A_c I_b \cos\theta (1 - \eta_{oel}) dt_S \tag{22}$$

Wherein, $t_{s,bt}$ and $t_{s,st}$ are the starting and finishing times of the experiment, respectively. η_{oel} signifies the optical end loss ratio of PTC [12]. The formula of the total cooling quantity is as follows:

$$Q_r = \int_{t_r,bt}^{t_r,st} m_{F,e} c_p (T_7 - T_8) dt \tag{23}$$

Wherein, $t_{r,bt}$ and $t_{r,st}$ are the operating and stopping time of the cooling chiller, respectively. The average cooling efficiency is expressed as follows:

$$\eta_{r,av} = \frac{Q_r}{\int_{t_r,bt}^{t_r,st} m_{F,g} c_p (T_5 - T_6) dt} \tag{24}$$

The function of $COP_{s,av}$ is shown as follows:

$$COP_{s,av} = \frac{Q_r}{E_{i,tot}} \tag{25}$$

From Table 9, it can be seen that the average cooling efficiency ($\eta_{r,av}$) and the average COP ($COP_{s,av}$) of the whole system were relatively low under the condition of cloudy weather. In such weather condition, solar radiation was relatively small. In consequence, hot water could not be heated to a high temperature. In addition, when the sun was covered by clouds, the pump ran at a fixed frequency all the time, which resulted in more pipeline heat losses. Therefore, the average cooling efficiency and the mean COP of the system were relatively low. In contrast, the cooling efficiency and COP of the system were high under clear weather conditions. The experiment results reveal that the average cooling efficiency of the chiller changed between 0.17 and 0.60, and the cooling coefficient of the whole system ranged from 0.11 to 0.27.

Solar Photovoltaic Cooling System

Background

The cooling demand of people increases continuously with the development of economy and the improvement of living standard, especially in hot summers. Therefore, there is a supply shortage of electric power in cities, and power blackout phenomenon still happens. Recently, the cooling driven by solar energy has become one of the promising approaches to reduce or partially replace conventional cooling systems. In the area of photovoltaic cooling, thermoelectric cooling and vapor compression cooling are two main cooling methods. Early in 2003, Dai et al. [49]

researched the thermoelectric refrigerator driven by solar cells. The results show that the system had a COP of 0.3 and the refrigerator temperature could maintain in a range of 5–10 °C. Due to the limitation of working principle, thermoelectric refrigerator is only suitable for cold storage instead of freezing. The vapor compression cooling driven by photovoltaic energy has attracted many researchers' attention. The vapor compression refrigerator driven by the power generated by the PV modules rather than grid power can reduce the dependence on city power and effectively alleviate the pressure on power grid. Nowadays, the photoelectric conversion efficiency of the PV modules has increased and the power generation cost of the PV modules has decreased year by year, with the development of photovoltaic technology. In addition, compared with thermal cooling, solar photovoltaic cooling has the advantages of stable operation and high cooling efficiency. Consequently, the researches on the vapor compression cooling driven by photovoltaic energy are under the spotlight all over the world.

A transformation refrigerator driven by power grid was upgraded by Kaplanis et al. [50], which could be driven by power grid and photovoltaic energy. The performance of this system was also analyzed. Aktacir [51] designed a multifunctional photovoltaic refrigerator and found that the minimum temperature of the refrigerator driven by photovoltaic energy reached −10.6 °C. It was reported that the performance variation coefficient of the cooling system decreased with the decrease of evaporating temperature [52]. Thus, it was very important to improve cooling performance through the control of the appropriate evaporation temperature. Modi et al. [53] conducted a study on the energy conversion, management, and operation performance of PV refrigerator system powered under three conditions, namely photovoltaic components, battery, and outage. The results indicate that the COP of this system decreased gradually from morning to night. DC compressor was applied in the photovoltaic refrigerator by Ekren et al. [54]. They found that the conversion efficiency of the PV modules would have a great impact on the exergy efficiency of the whole system. Mba et al. [55] utilized MATLAB software to simulate the operating process of PV cooling system and analyze its operating characteristics under different conditions. Furthermore, Tina et al. [56] designed software for monitoring and managing stand-alone PV refrigerator system in a remote area, which had a real-time monitor running status and automatically recorded data fed back to the terminal equipment. According to a comprehensive analysis, batteries are essential components for storing energy and avoiding the intermittence of solar energy in PV cooling system. However, batteries would not only increase investment and running costs but also reduce system energy conversion and utilization ratio.

In this background, Axaopoulos et al. [57] designed a PV ice-maker without battery, and studied its performance when the operating efficiency of the compressor was 9.2%. They found that this prototype had a good ice-making capability, a reliable operation, and a great improvement in the startup characteristics of compressors, which could remain working even on the days with a low solar irradiation of 150 W/m^2. Nevertheless, four compresses were adopted in parallel. Additionally, investment and operation costs were high, and system control strategy was complicated. Consequently, the ice storage technology with low cost and stable

performance has attracted the attention of researchers. Ice storage technology plays a great role in saving building energy, transferring peak power to off-peak power, improving grid load rate, and other aspects applied to many projects. The ice thermal energy storage (ITES) air-conditioning system incorporating a phase change material (PCM) was analyzed in terms of energy, exergy, economic, and environmental aspects [58]. On the basis of the results, the electricity consumption of hybrid system was 6.7% and 17.1% lower than that of the simple ITES (without PCM) system and the conventional system, respectively. Pu et al. [59] found that the total cumulative exergy consumption increased as the ITES system was applied. Moreover, the payback period of ITES system for extra capital cost was 3.43 years [60]. Based on the above analysis, ITES has a good economic and stability performance. In view of this, ice storage air-conditioning can be widely used. American SOLUS Cooling Company developed a photovoltaic DC refrigerator, substituting water-propylene/ethylene glycol phase change material for battery to store coldness and reduce the investment and running cost of the system. The results disclose that the temperature inside the refrigerator remained stable at around 1.4 °C when the environment temperature was 32 °C. Recently, the PV cooling system has been improved and developed in the aspects of product structure, operating efficiency, and cooling performance.

According to applications, traditional steam compression cooling system mainly consists of ice maker, refrigerator, and air-conditioning. Its driving energy is mainly from power grid, and composite energy system is composed of photovoltaic, battery bank, and distributed photovoltaic energy system.

Refrigerator Driven by Photovoltaic and Battery

Working Principle of Solar Photovoltaic Refrigerator

Solar photovoltaic refrigerator consists of photovoltaic modules, controller, inverter, battery bank, and household refrigerator. Its working principle is shown in Fig. 18.

In sunshine, the solar irradiance accepted by the photovoltaic module is transformed into direct current power. Part of the direct current power is converted into alternating current power by the inverter to drive the refrigerator and surplus electricity stored in the battery bank. The electrical energy output or storage process is controlled by the controller. In rainy weather or at night, the lacked electricity for driving the refrigerator is supplied by the battery bank, because the power generated by the PV modules is not enough to drive the refrigerator. In this research, the experimental platform of solar photovoltaic refrigerator was constructed, and its system performance was tested experimentally. The photo of the solar photovoltaic refrigerator is given in Fig. 19.

The tested refrigerator is a common AC refrigerator manufactured by some companies. Its main parameters are listed in Table 10.

The rated power consumption per hour of the refrigerator is 0.32 kWh/24 h. The total heat load of the refrigerator Q_z includes heat leakage loss Q_b, door opening loss Q_A, storage heat loss Q_p, and other heat loss Q_M. Their equation is shown below:

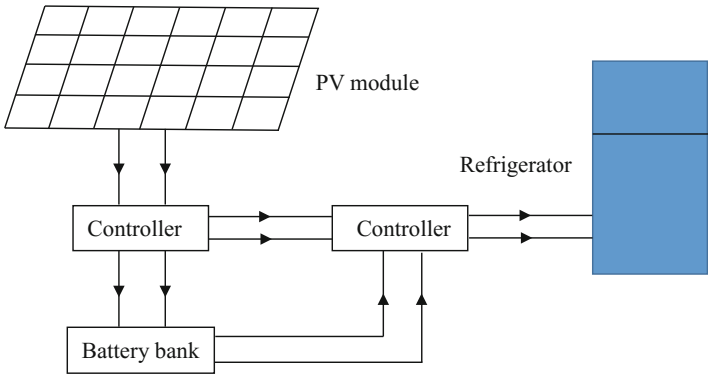

Fig. 18 Working diagram of solar photovoltaic refrigerator

Fig. 19 Photo of solar photovoltaic refrigerator

$$Q_z = Q_b + Q_A + Q_p + Q_M \tag{26}$$

The heat leakage loss Q_b contains the heat leakages of the freezer room Q_1, the storage room Q_2, the door seal Q_3, and the heat channel in the box structure Q_4. Their formula is as follows:

$$Q_b = Q_1 + Q_2 + Q_3 + Q_4 \tag{27}$$

The foaming insulation layer of the refrigerator plays the main thermal insulation function. The heat transfer mode of the freezer room wall can be simplified as that of single-layer flat wall. Hence, the heat leakages of the freezer room Q_1 and the storage room Q_2 can be calculated by:

$$Q_{1,2} = K_{1,2}F_{1,2}\left(T_a - T_{d,c}\right) \tag{28}$$

Table 10 Main parameters of refrigerator

	Value	Unit
Rated voltage	220	V
Rated current	0.6	A
Cryogen	R134a	
Outline size	524*588*1165	mm
Rated power consumption	13.33	0.32 kWh/24 h
Freezer room	35	L
Storage room	77	L

K_1 (m^2) denotes the outer surface area of the freezer room, and its measured value is 0.145 m^2, and F_1 (m^2) represents that of the storage room, and its measured value is 0.345 m^2. T_a (K) is the environment temperature around the refrigerator. T_d (K) indicates the freezer room temperature, and the set value is 253.15 K. T_c (K) signifies the storage room temperature, and its set value is 268.15 K. K_1 and K_2 are the heat transfer coefficients. W/(m^2·K) can be calculated by [61] :

$$K_{1,2} = \frac{1}{\frac{1}{\alpha_1} + \frac{\delta_{d,c}}{\lambda} + \frac{1}{\alpha_{2,3}}} \tag{29}$$

In the formula, α_1 is the surface heat transfer coefficient of the outer surface of the refrigerator, and its measured value is 20 W/(m^2·K). α_2 stands for the surface heat transfer coefficient of the inside surface of the freezer room, and its measured value is 3 W/(m^2·K). α_3 denotes that of the inside surface of the storage room, and its measured value is 2 W/(m^2·K). δ_d is the thickness of the outer wall of the refrigerator, and δ_c that of its inner wall. Their measured values are 0.095 m and 0.08 m, respectively. λ signifies the heat transfer coefficient of the cyclopentane (C_5H_{10}) of the refrigerator foaming layer, and its measured value is 0.095 m.

It is difficult to obtain the heat leakages of the door seal Q_3 with computational method. According to the experiment, Q_3 is generally about 10~20% of the sum of Q_1 and Q_2. The reference values given in the references [62, 63] are 15% and 17%, respectively. Q_3 is 10% of the sum of Q_1 and Q_2.

Valve-regulated lead acid free maintenance battery was applied to the battery bank, and the rated voltage of the battery was 12 V. As the inverter's input voltage was 24 V, the battery bank was made up of two batteries in series. The main parameters of the battery bank are given in Table 11.

The model of the monocrystalline silicon photovoltaic module selected in the system was JN-190 W. The relative parameters provided by the manufacturer are shown in Table 12. Tables 13 and 14 list the relative parameters of the controller and inverter provided by manufacturers, respectively.

Since the operating characteristics of the photovoltaic refrigerator system would vary with the daily solar irradiance, solar irradiance was tested during the experiment. In addition, the operating characteristics of the photovoltaic and battery bank were directly affected by the ambient temperature. Given this, the change of the

Table 11 Main parameters of battery bank

Parameters	Value
Rated voltage	12 V
Rated capacity	100 Ah
Number	2

Table 12 Main parameters of PV module

Parameters	Value
Peak power	190 W
Maximum power point voltage	36.3 V
Maximum power point current	5.23 A
Open-circuit voltage	45.3 V
Short-circuit current	5.55 A
PV module size	1.58 m*0.81 m

Table 13 Main parameters of controller

Parameters	Value
Rated voltage	24 V
Rated current	$\leq$15 A
Undervoltage protection voltage	22.4 V
Overcharge protection voltage	28 V
Overvoltage protection voltage	31 V

Table 14 Main parameters of inverter

Parameters	Value
Rated power	1000 W
Input voltage	24 V_{DC}
Output voltage	220 V_{AC}
Overcharge protection voltage	28 V
No-load current	0.3 A
Output frequency	50 Hz $\pm$ 0.5 Hz
Output waveform	Pure sine wave
Waveform distortion	THD $<$ 3% (linear load)
Undervoltage alarm	21 $\pm$ 0.5 V
Undervoltage/overvoltage protection	20 $\pm$ 0.5 V/31 $\pm$ 0.5 V
Undervoltage/overvoltage recovery	24 $\pm$ 0.5 V/29.5 $\pm$ 0.5 V

environment temperature and the working condition of the PV modules and the battery bank were monitored in real time. FD-1 type power test system, TRM-2 type solar water heater test system, and TBQ type solar pyranometer were applied in this experiment as the main test equipment.

Experimental conditions:

1. The refrigerator and test equipment were all in the room and their surfaces were insulated. The whole room had only one window for illumination.
2. The temperature controller in the refrigerator was set in the third gear. When the freezer room temperature dropped to −22 °C and the storage room temperature was reduced to 5 °C, the compressor shut down automatically.
3. In order to ensure that more solar irradiance could be accepted by the photovoltaic module, the installation direction of the PV modules was south and the dip angle was 25°.
4. In each experiment, the refrigerator door should be opened to ensure that its inside temperature was similar to the ambient temperature.

Experimental Test and Performance Analysis

Experimental Research on Solar Photovoltaic Refrigerator System Under Different Working Conditions

Analysis of the Results on an Experimental Day with Clear Weather

The changes of solar irradiance on an experimental day are shown in Fig. 20. On that day, sunrise time was 6:23, midday time 12:43, and sunset time 17:58. As the mounting angle of the solar panel was fixed, the solar irradiance accepted by the PV module reached the maximum value 974 W/m^2 at 13:13. The cumulative value of sunshine time all day was nearly 7 h, and the solar irradiance was higher than 350 W/m^2. The load of the refrigerator was 3 kg of water in the freezer room, and the storage room was empty. Three platinum resistance temperature sensors were adopted to monitor ambient temperature, storage room temperature, and water temperature. The changes in the temperature of the freezer room and the storage room of the refrigerator as well as ambient temperature are displayed in Fig. 20.

In accordance to Fig. 21, the temperatures of freezer room and storage room decreased step by step. It costed nearly 60 min for the temperature in the freezer room to drop from ambient temperature to 0 °C. Meanwhile, it costed nearly 180 min for the temperature in the storage room to decrease from ambient temperature to 5 °C. Figure 22 presents the changes in the voltages of the PV module and the battery bank. The voltage of the PV module varied with the changes of the solar irradiance, and the voltage of the battery bank increased gradually from 24 V to 25.6 V. This reveals that the electricity generated by the PV module was enough to drive the refrigerator, and the surplus electricity was stored in the battery bank.

Analysis of the Results on an Experimental Day with Cloudy Weather

The changes of solar irradiance on the day with cloudy weather are given in Fig. 23. Figure 24 displays the temperature changes of the freezer room, the storage room, and the ambient. Figure 25 presents the changes in the voltages of the PV module and the battery bank.

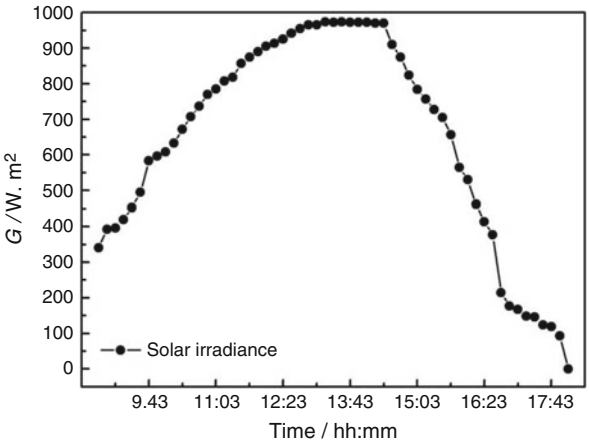

Fig. 20 Changes of solar irradiance on a sunny experimental day

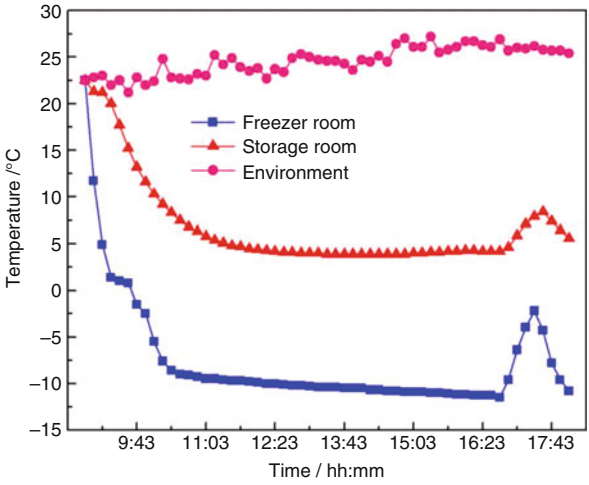

Fig. 21 Temperature changes of freezer room, storage room, and ambient temperature

It was observed that the voltages of the PV module and the battery bank fluctuated greatly. When the voltage of the PV module decreased with the drop of the solar irradiance, the voltage of that battery bank increased. After the experiment, the voltage of that battery dropped by 1.5 V. It reveals that the electricity generated by the PV module was not enough to drive the refrigerator, and the lacked electricity was supplied by the battery bank.

Analysis of the Results on an Experimental Day with Overcast Weather

The temperature changes of the freezer room, the storage room, and the ambient are shown in Fig. 26. The changes in the current and voltage of the battery bank are given in Figs. 27 and 28, respectively.

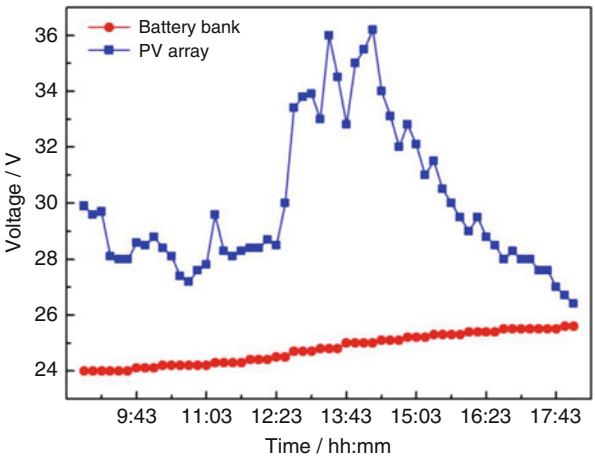

Fig. 22 Voltage changes of PV module and battery bank

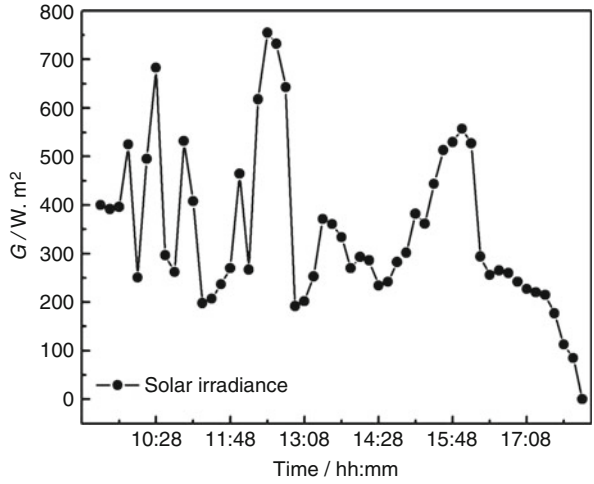

Fig. 23 Changes of solar irradiance on a cloudy day

From Fig. 26, it can be observed that the temperature in the freezer room of the refrigerator declined gradually, and the minimum temperature after the experiment reached −22 °C. The temperature in the storage room of the refrigerator changed periodically between 0 °C and 7 °C. Figures 27 and 28 uncover that the refrigerator operated periodically as well. The experimental results manifest that the refrigerator started seven times during the experiment. On account of this, a very important parameter, i.e., the running rate of the refrigerator, was expressed with B and introduced to evaluate the quality of the refrigerator, which can be calculated by the formula below [64] :

$$B = \frac{T_1}{T_1 + T_2} \tag{30}$$

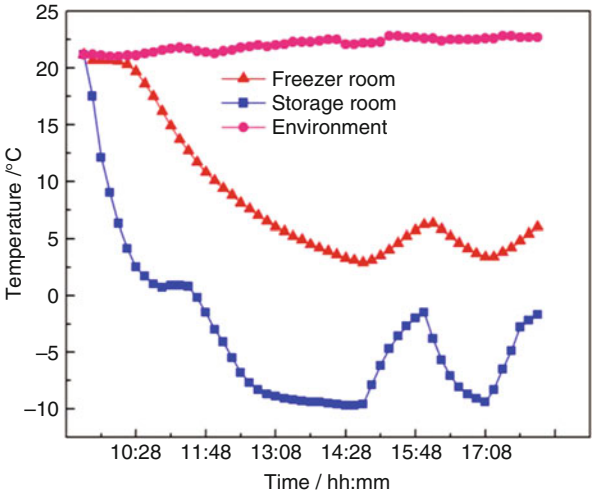

Fig. 24 Temperature changes of freezer room, storage room, and ambient

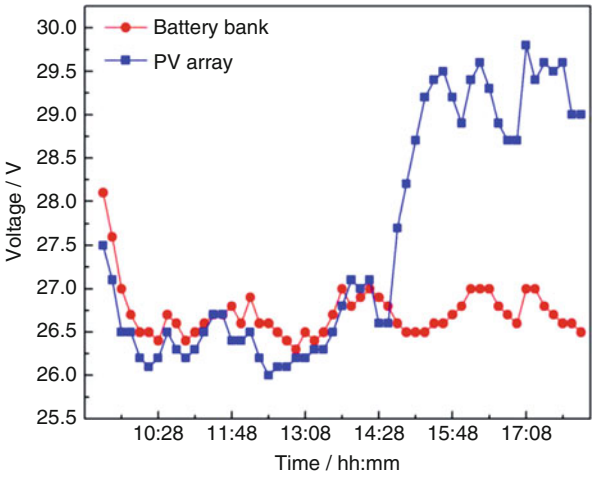

Fig. 25 Voltage changes of PV module and battery bank

In the formula, T_1 and T_2 (s) are respectively the operation time and shutdown time of the refrigerator. According to the manufacturer, the rated average boot time and downtime in every work cycle of the refrigerator were 20 min and 42 min, respectively. The running rate of the refrigerator calculated by formula 30 was 32%. Based on the experimental data, the running rate of the refrigerator on sunny days and cloudy days were 38% and 36%, respectively.

Research on the Load Characteristics of Photovoltaic Refrigerator System

No-Load Characteristics of Photovoltaic Refrigerator System

There was nothing in the freezer room and the storage room of the refrigerator. The experiment test work lasted 24 h. The temperature changes of the freezer room and

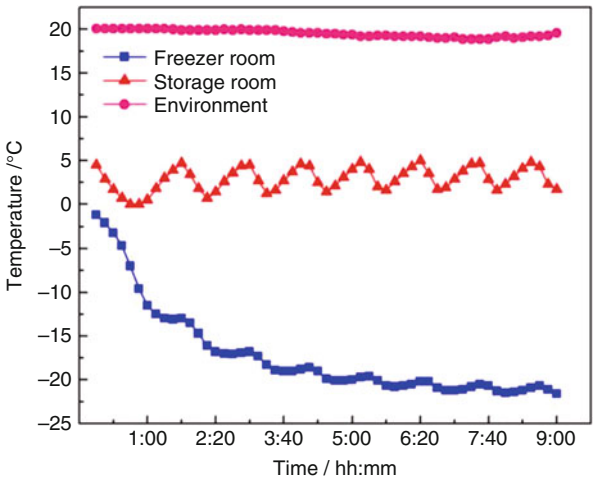

Fig. 26 Temperature changes of freezer room, storage room, and ambient

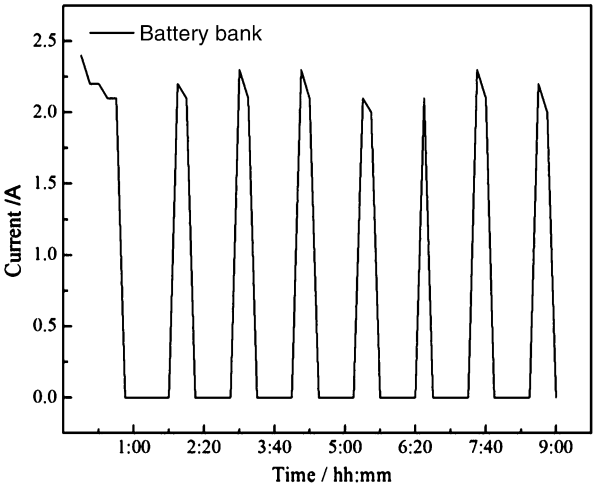

Fig. 27 Changes in the current of battery bank

the storage room of the refrigerator are shown in Fig. 29. The exhaust temperature of the compressor was also monitored, which is exhibited in Fig. 29.

As can be seen from Fig. 29, the temperatures of the freezer room and the storage room firstly decreased step by step. When the refrigerator operated stably, the temperatures of the freezer room and the storage room changed periodically. However, the temperature of compressor firstly increased. When the refrigerator operated stably, the temperature of compressor gradually decreased periodically. It costed nearly 75 min for the temperature in the freezer room to drop from ambient temperature to 0 °C. Meanwhile, it costed nearly 150 min for the temperature in the storage room to reduce from ambient temperature to 5 °C. After 210 min, the refrigerator entered a stable operation stage.

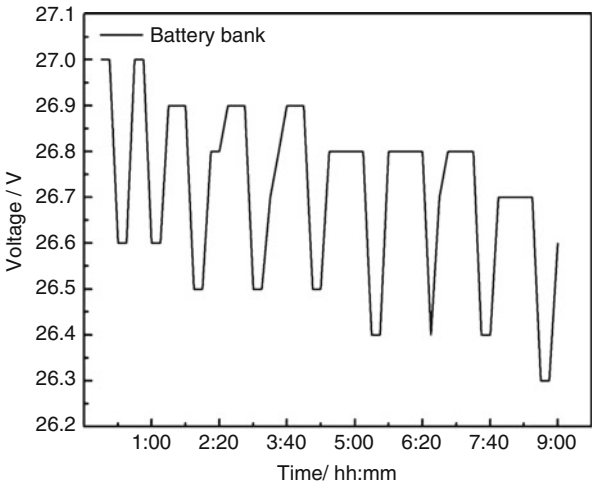

Fig. 28 Changes in the voltage of battery bank

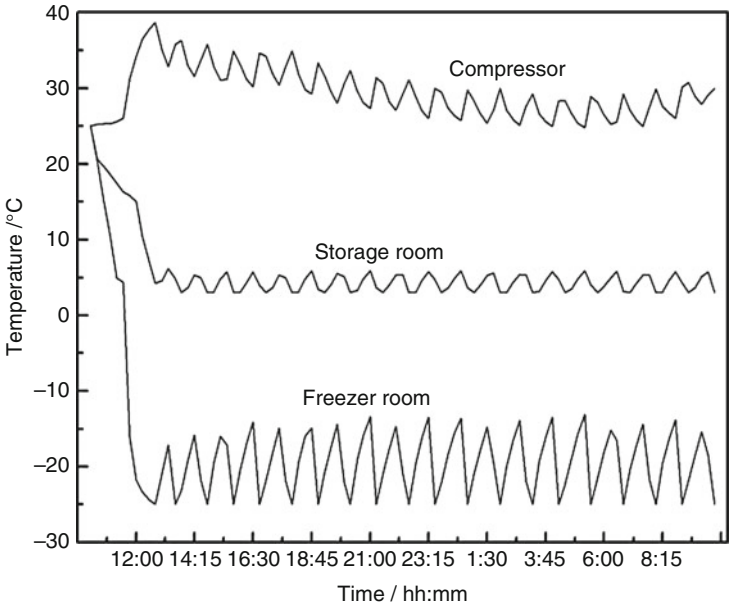

Fig. 29 Temperature changes of freezer room, storage room, and exhaust

Figure 30 shows the changes in the voltages of the PV module and the battery bank. The voltage of the PV module varied with the changes of the solar irradiance, and the voltage of the battery bank increased gradually from 24 V to 25.6 V. This reveals that the electricity generated by the PV module was enough to drive the refrigerator, and the surplus electricity was stored in the battery bank. The changes in the currents of the PV module and the battery bank are given in Fig. 25. It can be

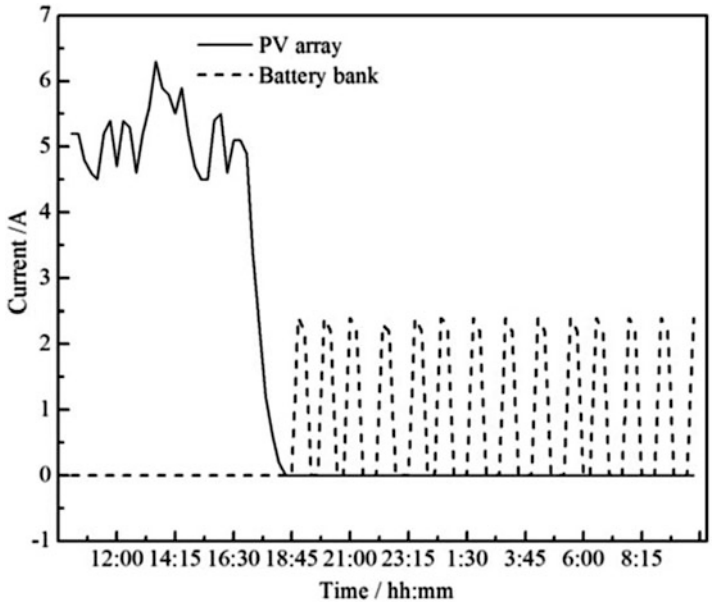

Fig. 30 Current changes of PV module and battery bank

observed that the refrigerator could be driven by the PV module only on sunny days. During night, the refrigerator was driven by the battery bank. The current of the battery bank varied periodically between 2.1 A and 2.4 A. The calculated running rate of the refrigerator was 28%.

Operating Characteristics Analysis of the Photovoltaic Refrigerator with Different Loads

The operating characteristics of the photovoltaic with three different loads, i.e., 5 kg, 6 kg, and 7 kg of water in the freezer room, were tested through an experiment. During the experiment, the cumulative solar irradiance accepted by the PV module was limited to 10 MJ. As the refrigerator had two stages, i.e., cooling and periodic stable operation, the operating characteristics of the refrigerator with the three different loads were analyzed in two stages.

(a) Cooling stage

The temperature changes of the three loads, i.e., 5 kg, 6 kg, and 7 kg of water, in the refrigerator freezer room in the cooling process are given in Fig. 31. The time for water temperature to decrease from ambient temperature to 0 °C under the condition of the three loads was 110 min, 180 min, and 220 min, respectively. Figure 32 shows the temperature change curves of the compressor with the three different loads. It was revealed that the operating temperature of the compressor increased with the increase of the loads.

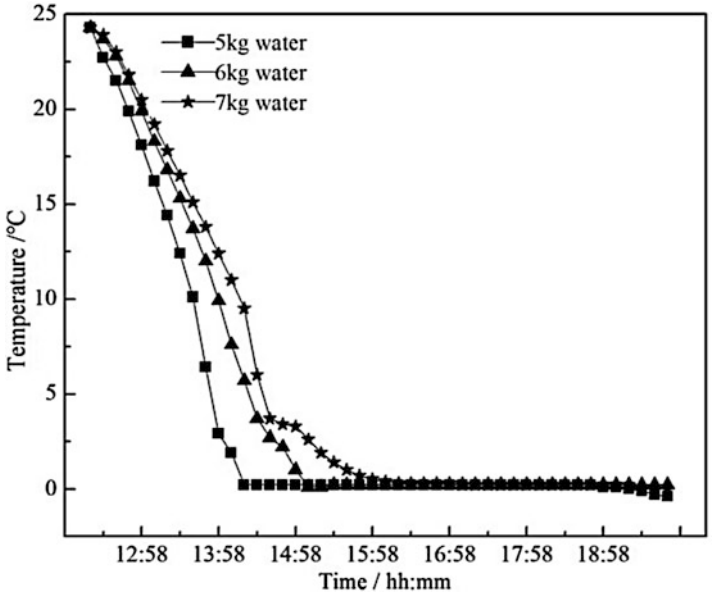

Fig. 31 Current changes of PV module and battery bank

The cooling coefficient of performance (COP) was used to judge the cooling performance of the refrigerator. Generally, the COP was expressed with the ratio of cooling capacity Q to the solar energy Q_s received by the PV modules. It can be obtained by using the formulas below:

$$COP = \frac{Q}{Q_s} \tag{31}$$

$$Q = c_1 m_1 \Delta t_1 + \gamma m_2 + c_2 m_2 \Delta t_2 \tag{32}$$

$$Q_s = IA \tag{33}$$

In the above formulas, c_1 is the specific heat capacity of water (4.2×10^3 J/kg °C). m_1 is the weight of water (kg). Δt_1 denotes the temperature variation of water (°C), and γ the change of latent heat in the water phase (335 kJ/kg). m_2 signifies the weight of ice (kg). Δt_2 represents the temperature variation of ice (°C), and I the cumulative solar irradiance, MJ/m^2. A indicates the total area of the PV module (m^2). The changes in the COP of the refrigerator with three different loads are shown in Fig. 33.

From Fig. 33, it can be seen that the COPs of the system with 5 kg, 6 kg, and 7 kg of water loads increased gradually. At 13:58, the COPs of the three loads reached the maximum values, i.e., 0.27, 0.18, and 0.25, respectively. Then, they decreased step by step. In accordance to Formulas 31-33, COPs depended on the weight and temperature of the loads when the accumulated irradiance remained constant.

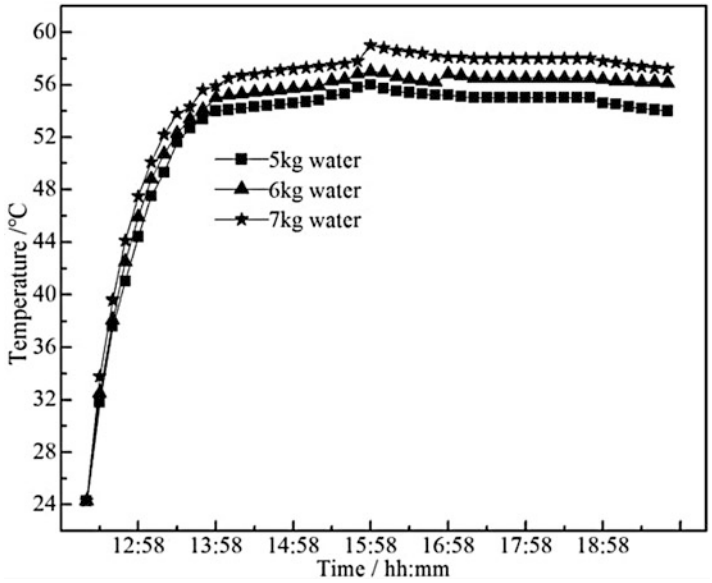

Fig. 32 Temperature change curves of compressor with different loads

(b) Stable operation stage

Figure 34 displays the temperature changes of the system with the three loads when the refrigerator gradually entered into the stable operation stage from cooling stage. From the Fig. 34, the time for water temperature to decrease from ambient temperature to −20 °C under the condition of the three loads was 791 min, 1151 min, and 1232 min, respectively. These results suggest that different loads would need different condensation time [65] .

Under the condition of the same cumulative irradiance (10 MJ), the operation characteristics of the refrigerator with three different loads are compared in Table 15.

Air-Conditioning Driven by Photovoltaic Energy with Battery

Working Principle of the Air-Conditioning System Driven by Photovoltaic Energy with Battery

Distributed photovoltaic air-conditioning system mainly consists of photovoltaic modules, controller, inverter, and air-conditioning. The diagram of its working principle is shown in Fig. 35. The electricity generated by the PV array is direct current, which is converted into alternate current by the inverter to drive the air-conditioning system. The surplus power would be stored in the battery bank, and the flow of electricity is controlled by the controller. The electricity stored in the battery bank can be discharged to drive air-conditioning system, when solar irradiance is low or there is no solar irradiance at all.

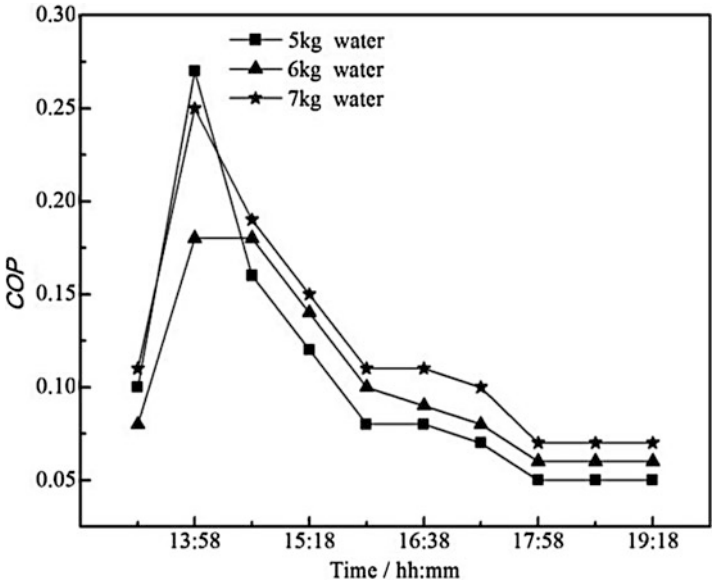

Fig. 33 Changes in the COPs of PV module and battery bank

Air-Conditioning System Driven by Photovoltaic Energy with Battery

Calculation of Indoor Cold Load

The air-conditioning system driven by photovoltaic energy with battery was applied to serve an office room located in the night side. Its effective area was 23.3 m^2, and its volume was 88.3 m^3. With an enclosure structure, it was mainly composed of wooden wall for partition, as well as glass wall and concrete wall. The controller, inverter, and other equipments are placed indoor, and the PV array was fixed outdoor [27, 66]. The real picture of the room is shown in Fig. 36. Its cold load was calculated and given in Table 16.

Air-Conditioning

The cold load of the office room was calculated to be 1971.4 W. Therefore, a 1.5 HP variable frequency air-conditioning was selected in this research, according to the cold load and the detailed parameters of the air-conditioning system, which are listed in Table 17.

Photovoltaic Module

The characteristics parameters of the PV module adopted in the system are displayed in Table 18. The model of the PV module is JN-DJB-245.

Since the rated voltages of the inverter, the controller, and the battery bank are 48 V, and the floating charge voltage of the battery bank is 57.6 V, the output voltage of the PV array should be higher than 57.6 V most of the time. For this reason, the PV

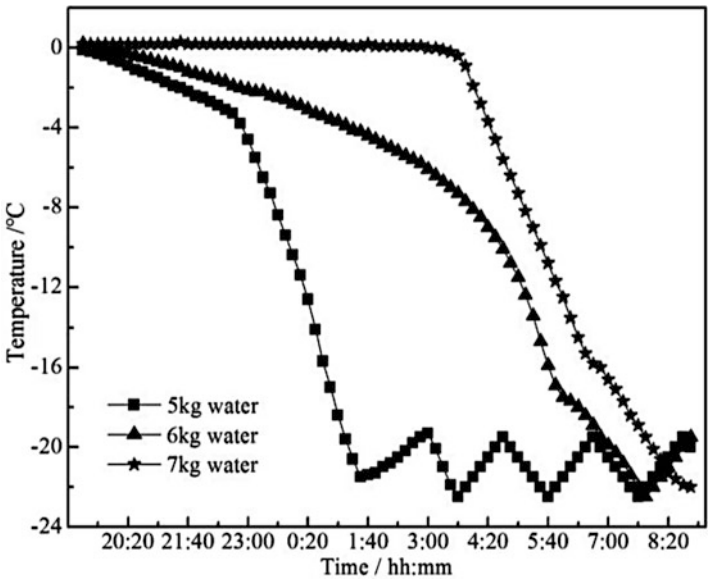

Fig. 34 Temperature changes of three different loads

Table 15 Operation characteristics of the refrigerator with three different loads

Load (water, kg)	Power consumption (kWh)	Refrigerator operating rate (%)	COP
5	1.1	38.50	0.24
6	1.9	42.80	0.29
7	2.1	46.70	0.32

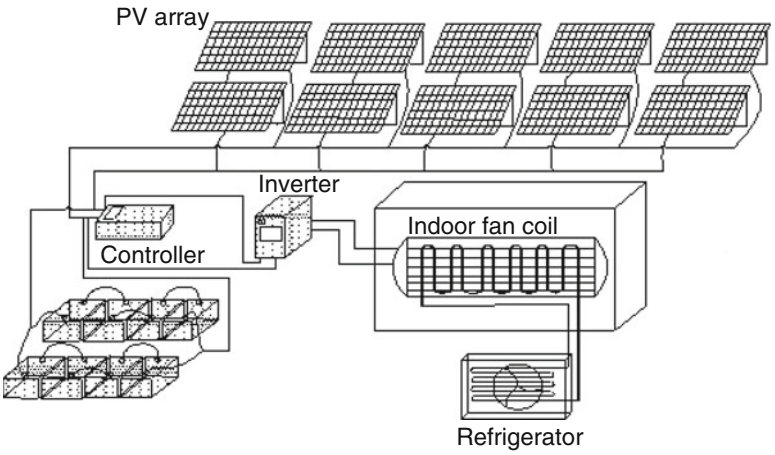

Fig. 35 Working principle of distributed photovoltaic air-conditioning system

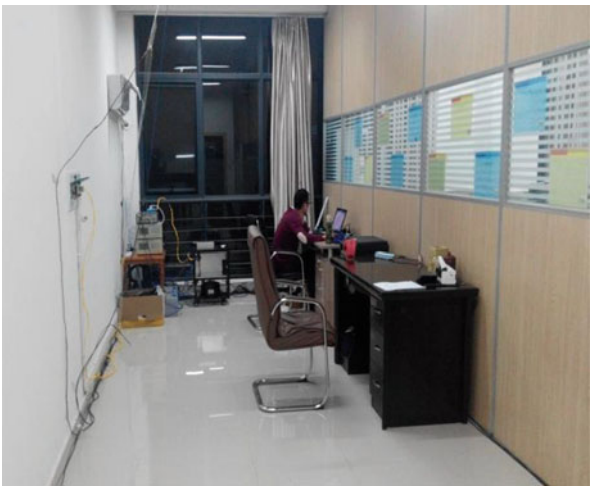

Fig. 36 Cooling load (office room)

modules should be connected with two PV modules in series and five series in parallel. The peak rated power of the PV array is 2.45 kW.

Inverter

The capacity of the inverter can be calculated according to the formula below:

$$C_n = \frac{P_L}{P_F \cdot \eta_{inv}} \tag{34}$$

Wherein, C_n is the capacity of the inverter, and P_L is the load power, which is the operation power of the air-conditioning. Its tested value is 2270 W. P_F represents the power factor of air-conditioning load, and its tested value is 0.85. η_{inv} indicates the efficiency of the inverter. Its rated value is 93%, according to the manufacturer.

On this basis, the calculated C_n is 2.97 kVA. Therefore, a normal capacity of 3KVA KFNB48-3000C was adopted. The main parameters of the inverter are exhibited in Table 19.

Battery Bank

The valve-regulated maintenance free lead-acid battery was adopted. As the DC voltage of the system was 48 V and the rated voltage of a single battery was 12 V, four batteries were connected in series in order to provide a voltage of 48 V. To ensure that the air-conditioning system would normally and persistently operate for 8 h during the day, the capacity of the battery bank should be 130 Ah. In the light of this, the battery bank was made up of four batteries in series and two series in parallel with a rated capacity of 130 Ah.

Table 16 Cold load of office room

Enclosure structure			Heat transfer coefficient	Setting value of the different temperature between indoor and outdoor	Temperature correction factor	Cold load	Total cold load
Name and direction	Size (m × m)	Area (m^2)	K (W/m^2 °C)	t_w–t_n (°C)	α	Q′ (W)	Q (W)
East wall (wooden partition)	8.3 × 2.8	23.24	0.2	6	1	27.888	
East wall (glass)	8.3 × 0.64	5.312	1.2	6	1	38.2464	
East wall (concrete)	8.3 × 0.36	2.988	1.8	6	1	32.2704	
West wall (concrete)	8.3 × 3.8	31.54	1.8	6	1	340.632	
South wall (wooden door)	2 × 1.4	2.8	0.2	5	1	2.8	1971.39
South wall (glass)	1.92 × 0.59	1.133	1.2	5	1	6.798	
South wall (concrete)	2.8 × 0.81	2.268	1.33	5	1	15.0822	
North wall (concrete)	2.8 × 0.9	2.52	1.8	10	1	45.36	
North wall (glass)	2.8 × 2.6	7.54	1.2	10	1	90.48	
Ground	8.3 × 2.8	23.24	1.6	5	1	185.92	
Top	8.3 × 2.8	23.24	1.6	5	1	185.92	

Table 17 Characteristic parameters of the air-conditioning with variable frequency

Parameters	value
Rated frequency	1–50 Hz
Rated cooling capacity	3200 W
Rated wind volume of the indoor fan coil	600 m^3/h
Rated *COP*	4.25

Controller

Generally, the maximum current of the controller is determined by the maximum operation power of the air-conditioning, the maximum output current of the PV array, and the maximum output current of the battery bank. As a result, a 60 A

Table 18 Parameters of PV module

Parameters	Value
Maximum peak power	245 W
Maximum power point voltage	31.5 V
Maximum power point current	7.78 A
Open-circuit voltage	41.8 V
Short-circuit current	8.3 A
Peak power temperature coefficient	−0.45%/°C
Temperature coefficient of voltage	−0.34%/°C
Temperature coefficient of current	0.05%/C

Table 19 Parameters of inverter

Parameters	Value
Rated output power	3000 W
Maximum output power	3150 W
Input voltage	48 V
Output voltage	220 V
Output frequency	50 Hz
Automatic protection	Overload, short circuit, over temperature, reverse connection, undervoltage and overvoltage
Cooling form	Forced air cooling

controller was employed in the system, and PH0C0S-PL-60 was chosen as the model of the controller. The detailed parameter values of the controller are listed in Table 20.

The performance parameters of each component were designed. The detailed parameters of the PV air-conditioning system are shown in Table 21, and the constructed distributed PV air-conditioning system is presented in Fig. 37.

System Performance Evaluation Index

The COP and guarantee rate of the system are two main performance indexes for judging the performance of the PV air-conditioning. The COP of the system can be expressed as the ratio of the air-conditioning cooling capacity to the accumulated solar irradiance accepted by the PV array, as shown in Formula 35:

$$COP = \frac{Q_{nl}}{E_{nl}} = \frac{\int_{T_0}^{T_n} \int_{t_0}^{t_n} C_p \rho \dot{m}_a dT dt}{(E_0 + E_1 + \cdots + E_n) \times 60} \tag{35}$$

Table 20 Parameters of controller

Parameters	Value
Rated current	60 A
Rated voltage	48 V
Under voltage	42 V
Undervoltage recovery voltage	48 V
Overvoltage	57.8 V
Overvoltage recovery voltage	56 V
Float voltage	57.6 V
Static loss	≤0.09 W

Table 21 Component parameter list of distributed PV system

Component	Model	Parameter	Value
PV module	JN-DJB-245	Rated power	2.45 kW
Controller	PH0C0S-PL-60	Rated voltage	48 V
		Maximum current	60 A
Inverter	KFNB48-3000C	Rated voltage	48 V
		Rated capacity	3 kW
Battery bank	6-GFMJ-65	Rated voltage	48 V
		Rated capacity	130 Ah
Variable frequency air-conditioning	KFR-32G/(32580) FNX-A3	Cooling power	0.1–1.4 kW

The guarantee rate of the system can be expressed as the ratio of the output power of distributed hybrid energy system to the consumed power of the air-conditioning during the day, as shown below:

$$Z = \frac{E_{nl}}{Q_{ns}} = \frac{(E_0 + E_1 + \cdots + E_n) \times 60}{\int_{t_0}^{t_n} pd} = \frac{(E_0 + E_1 + \cdots + E_n) \times 60}{p_1 t_1 + p_2 t_2 + p_3 t_3 + \cdots + p_n t_n} \quad (36)$$

In Formulas 35 and 36, Q_{nl} is the cooling capacity, J. E_{nl} the accumulated solar irradiance accepted by the PV array, and E_i the accumulated solar irradiance accepted by the PV array per minute. J. C_p signifies the air specific heat (1.005 kJ/kg.k). $\dot{m}_a$ denotes the air volume out of the indoor fan coil (m^3/s). ρ represents the air density, (1.2~1.5 kg/m^3). T_0 and T_n are the instantaneous temperatures before and after the experiment, while t_0 and t_n are the time before and after the experiment.

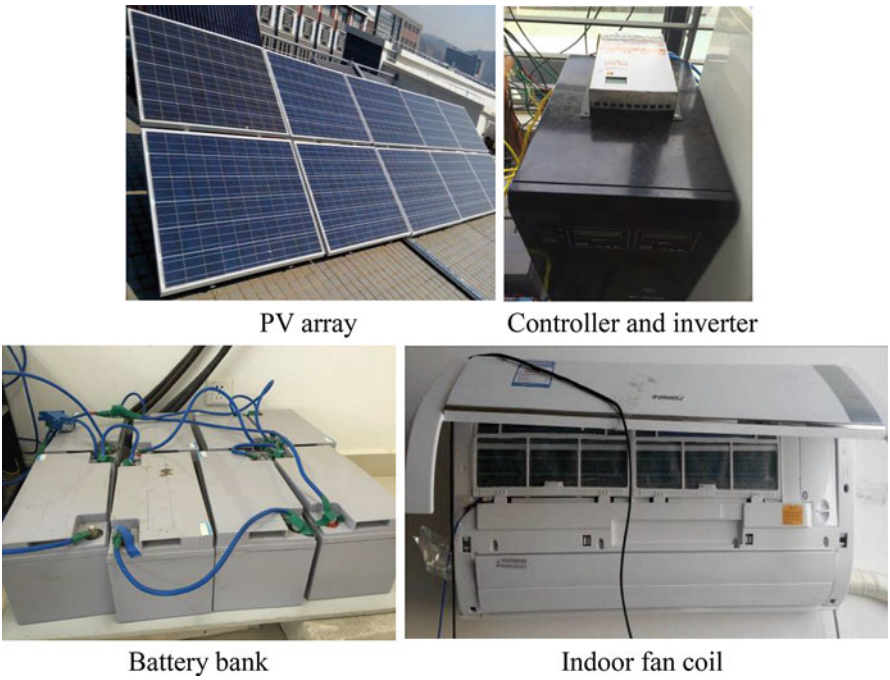

Fig. 37 1.5 PH distributed photovoltaic air-conditioning system

Performance Test and Analysis of Distributed Photovoltaic Air-Conditioning System

The operating current and voltage of the refrigerator, the output currents and voltages of the PV array, and the battery bank as well as the solar irradiance were tested through an experiment in Kunming. Based on the experiment data, the COP and guarantee rate of the system could be calculated. The operating performance test of the distributed PV air-conditioning system lasted for 1 year. The research results are shown in Table 22.

Cooling Performance Analysis of the Air-Conditioning Driven by Distributed Solar Photovoltaic Energy with Battery Bank

The operating performance of the system was tested during the period from 14:00 to 19:00. The setting temperature of the air-conditioning was 20 °C. The change curves of the solar irradiance, the output power of the PV array, and the operation power of the air-conditioning are displayed in Fig. 38. The change curves of ambient temperature, indoor temperature, evaporator temperature, and output temperature of indoor fan coil are presented in Fig. 39.

From Fig. 38, it can be observed that the solar irradiance decreased gradually after 14:00, and the maximum value was 842 W/m^2. At the same time, the output power

Table 22 Research results of distributed photovoltaic air-conditioning system

	April 2015	May 2015	June 2015	July 2015	August 2015
Daily average cumulative solar irradiance kW.h/m^2/d	6.19	5.5	5	4.51	4.22
Daily average electricity generated by PV array kW.h/d	13.00	11.55	10.50	9.47	9.09
Daily average temperature °C	18.35	19.92	20.47	20.35	20.13
Air-conditioning operation mode	Cooling	Cooling	Cooling	Cooling	Cooling
Average COP	0.35	0.34	0.37	0.36	0.34
Average guarantee rate	1.25	1.18	1.09	0.93	0.71

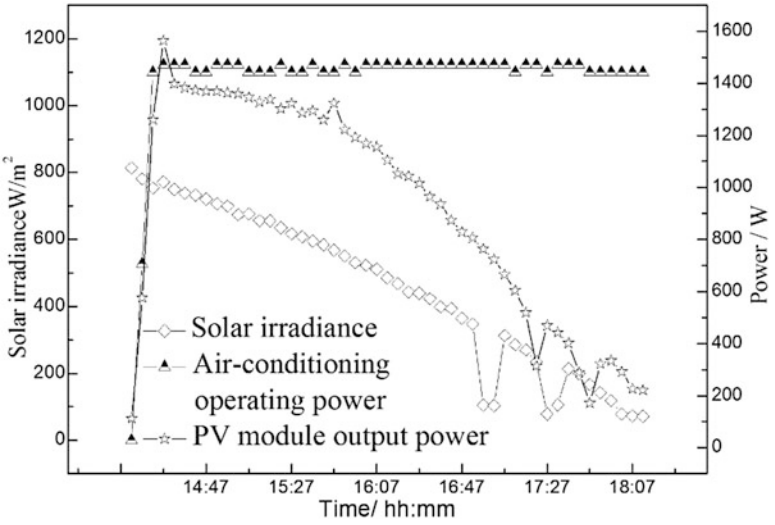

Fig. 38 Change curves of solar irradiance, PV output power, and air-conditioning consummation power

of the PV array decreased step by step as well, and the maximum output power generated by the PV array was 1598 W. The operation power of air-conditioning was maintained at about 1150 W. At about 16:10, the power generated by the PV array decreased to the same level of the consummation power of the air-conditioning. In accordance to Fig. 39, the minimum indoor temperature could only be reduced to 24.8 °C during the cold service process, when the temperature of the air-conditioning was set at 20 °C and the outdoor temperature was above 30 °C. In the experiment, the evaporator temperature was basically stable at about 13 °C, and the outlet temperature of the fan coil was about 20 °C. The poor sealing of the room and the serious cold leakage was the main reasons for the high indoor temperature, which could not decrease to the set temperature.

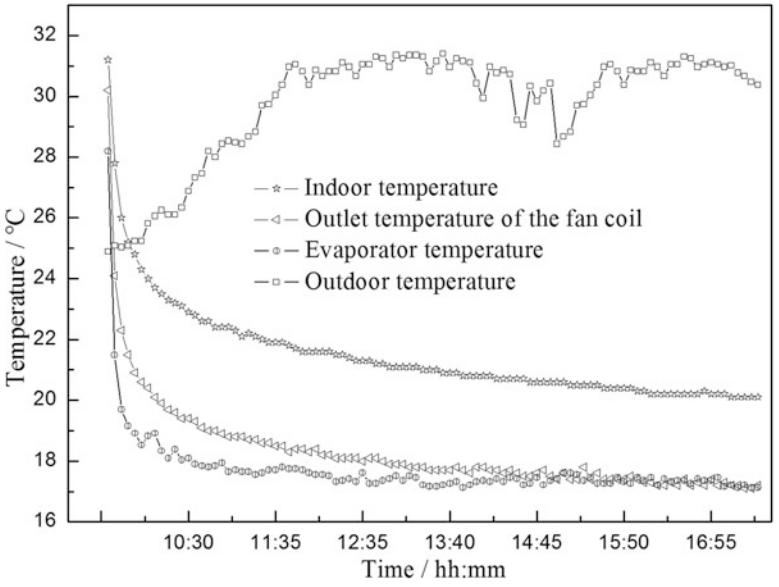

Fig. 39 Temperature change curves

Theoretical Analysis of the Energy Conversion and Transfer Characteristics of the Air-Conditioning System Driven by Distributed Photovoltaic Energy System with Battery Bank

Energy Models of PV Array

The output current of PV modules can be expressed as follows [66]:

$$I_P = MI_L - MI_O \left[\exp\left(\frac{q\left(NV + \frac{I_P R_S N}{M}\right)}{NAkT_P - 1} \right) \right] - \left[\frac{NV + \frac{I_P R_S N}{M}}{\frac{NR_{Sh}}{M}} \right] \tag{37}$$

Wherein, I_p is the output current of panel (A), I_L the light-generated current per module (A), and I_0 reverse saturation current per module (A). M denotes the number of module strings in parallel, N the number of modules in each series string, and V the terminal voltage of modules (V). R_s signifies the diode series resistance per module (ohms), R_{sh} the diode shunt resistance per module (ohms), and q the electric charge (1.6×10^{-19} C). k represents Boltzmann constant (1.38×10^{-23} J/K), A the diode ideality factor for the module, and T_p the cell temperature (K).

Based on Eq. 1, the output voltage of the panel will be zero under short-circuit condition, and the output current of the panel will be maximized, which is called short-circuit current and denoted as I_{sc}. In this condition, light-generated current will be equal to short-circuit current ($I_L = I_{sc}$), since R_s will be very small unless the lights

were concentrated. This model expresses I_{sc} as a function of solar irradiance and temperature [66].

$$I_L = I_{SC} = P_1 G\left[1 - P_2(G - G_r) + P_3\left(T_p - T_r\right)\right] \tag{38}$$

Wherein, P_1, P_2, and P_3 are constant coefficients for I_{sc}, which were achieved through experimental tests. G is solar irradiance (W/m^2), G_r reference solar irradiance (W/m^2), and T_r reference temperature (K). 1000 W/m^2 and 298 K were selected as reference solar irradiance and reference temperature respectively as normal.

Reverse saturation current was a small current flowing back through PV modules all the time. To estimate this current, an exponential expression was utilized, because it was a function of cell temperature as mentioned in Ref. [66]

$$I_O = BT_p^3\left[\exp\left(-\frac{E_{go}}{kT_p}\right)\right] \tag{39}$$

Wherein, E_{go} is a band gap energy at 0 K (1.16 eV for silicon), and B a material constant, which has to be estimated by using both the manufacturer's data and the I-V curve characteristics of PV modules.

The energy balance equation of PV modules is expressed as follows:

$$(mCp_{\text{module}})T_p = Q_{pv,in} - Q_{pv,rad} - Q_{pv,conv} - Q_{pv,elect} \tag{40}$$

Wherein, mCp_{module} is the effective thermal capacity of PV modules (W/K), $Q_{pv,in}$ the solar energy absorbed by PV modules (W), and $Q_{pv,rad}$ radiation heat loss (W). $Q_{pv,conv}$ indicates convective heat loss (W), and $Q_{pv,elect}$ electrical power (W).

The solar energy absorbed by PV modules can be estimated with the formation below:

$$Q_{pv,in} = \tau G S_p \tag{41}$$

τ is the product of cover glass transmittance, and G PV modules absorption rate, which can be tested in the experiment. S_p stands for the total area of PV modules (m^2).

Radiation heat loss can be obtained by using the following equation:

$$Q_{pv,rad} = S_p F_{ps}\sigma\left(\varepsilon_p T_p^4 - \varepsilon_s T_s^4\right) \tag{42}$$

F_{ps} is the sky view factor of the panel. Its value can be regarded as 1. σ denotes Stephan-Boltzmann constant (5.76×10^{-8} W·m^{-2}·K^{-4}), and ε_p the average emissivity of PV modules. Its value can be regarded as 0.8, ε_s signifies the average emissivity of sky, and its value can be considered as 1. T_s indicates the sky temperature (K), which is 0.914 times that of ambient temperature as suggested in [61].

Convective heat loss can be estimated with the following formula:

$$Q_{pv,conv} = S_p(T_p - T_a)\left\{1.2475\left[(T_p - T_a)\cos\beta\right]^{1/3} + 2.686V_{wind}\right\} \quad (43)$$

β is tilt angle (°), T_a ambient temperature (K), and V_{wind} wind speed (m/s).

Electric power can be expressed by [66]:

$$Q_{pv,elect} = GS_c\eta_0\left[1 - \gamma(T_p - T_r)\right] \quad (44)$$

S_c is the total surface area of PV cells (m^2), η_0 represents the efficiency of PV modules at a reference temperature, and γ the temperature transfer factor of PV conversion efficiency.

Energy Models of Air-Conditioning System

Figure 40 presents the thermodynamic cycle and cooling process of ice maker, i.e., refrigerant R134a, as well as its thermodynamic properties and *P-h* changing curve in the cooling cycle. It can be clearly seen from Fig. 40 that Area 1 is the saturated liquid region, Area 2 the gas-liquid coexistence region, and Area 3 the saturated vapor region. Consequently, the cooling cycle is 1-2-2s-3-4-5-1 across the saturated vapor region and gas-liquid coexistence region. The process from 1 to 2 is an actual working process of the compressor, when the dry steam in State 1 is compressed into saturated vapor in State 2, which will be isentropically compressed to 2s under an ideal condition. Nonetheless, Process 2-2s-3-4 is the refrigerant's condensing and heat releasing process in the condenser. Process 2-2s is the natural cooling process, and 2s-3-4 is the isobaric cooling process. The cryogen will become high-pressure dry steam in State 3, and high-pressure saturated liquid in State 4. Process 4-5 is the decompression and cooling process realized by throttle valve. Hence, the refrigerant temperature and

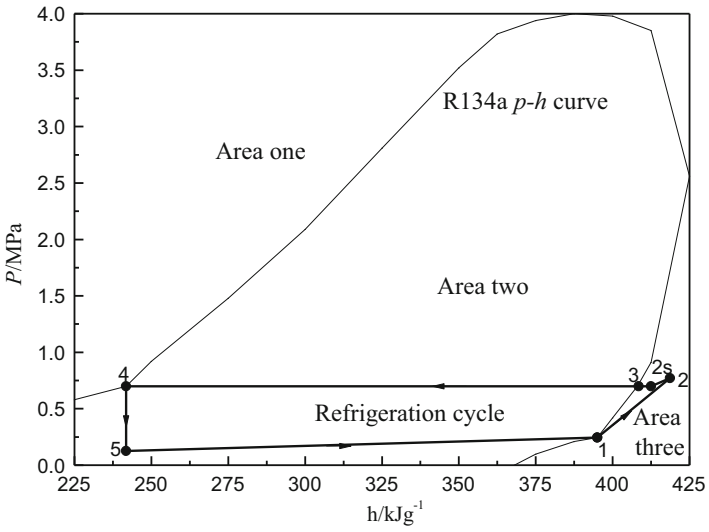

Fig. 40 Thermodynamic curve of R134a

pressure will become low after flowing through the throttle valve. Then, it can flow into evaporator to absorb heat and achieve refrigeration, which is Process 5-1.

Energy and exergy analyses are shown as follows:

(a) The compressor energy balance equation is given by:

$$\dot{m}h_1 + W_P = \dot{m}h_2 + Q_{CP,loss} \tag{45}$$

$\dot{m}$ is the refrigerant mass flow (kg/s). h_1 and h_2 represent the refrigerant enthalpy in State 1 and State 2, respectively (J/kg). W_p stands for compressor operating power (W), and $Q_{CP,loss}$ the compressor energy loss per unit time (W).

(b) The condenser' energy balance equation is as follows:

$$Q_{CP,out} = \dot{m}h_4 + Q_E \tag{46}$$

$Q_{CP,out}$ signifies the energy transmission from the compressor to the condenser per unit time (W), Q_E the condenser's rejection heat per unit time (W), and h_4 the refrigerant enthalpy in State 4 (J/kg).

(c) It is the isenthalpic throttling process of the refrigerant in throttle valve, so it can be expressed with the following equation:

$$Q_{CO,out} = Q_{TH,out} \tag{47}$$

$Q_{CO,out}$ is the condenser's output energy per unit time (W), and $Q_{TH,out}$ the throttle valve's output energy per unit time (W).

(d) The evaporator's energy balance equation is as follows:

$$Q_{TH,out} + Q_{AB} = Q_{CP,in} \tag{48}$$

Q_{AB} denotes the evaporator's absorption heat from water (W).

The thermal resistance network diagram of PV air-conditioning is shown in Fig. 41.

In Fig. 41, G is the solar irradiance accepted by the PV array. G_{mon} indicates the electricity generated by the PV array, G_k the energy that flowed through the controller, and G_b the energy of the battery bank. G_n represents the energy that flowed through the inverter, G_a the energy that flowed into the air-conditioning, and G_0 the energy in the door.

Theoretical Calculation and Analysis

The MATLAB programming was utilized to simulate the running process of the system. The calculation process is shown in Fig. 42, and the calculated results are given in Fig. 43.

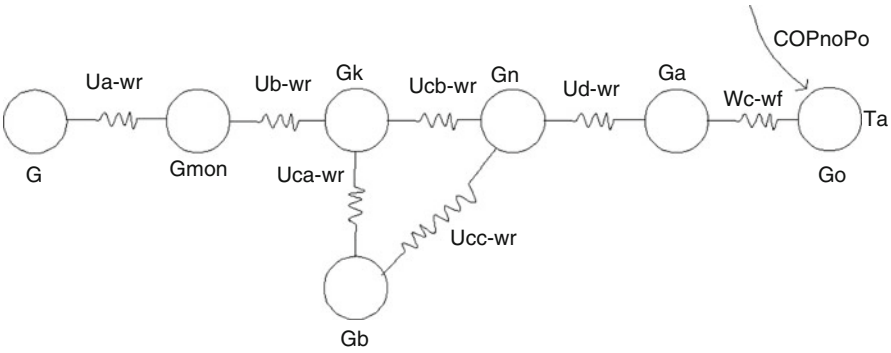

Fig. 41 Thermal resistance network diagram of PV air-conditioning

Fig. 42 Calculation process

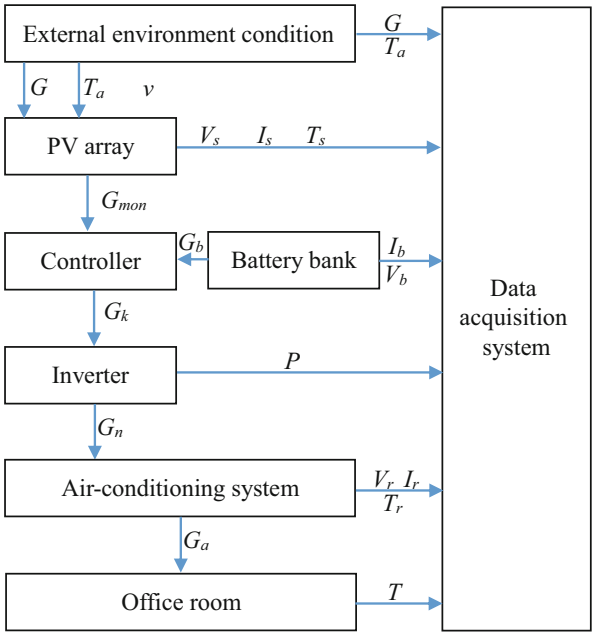

The simulated results displayed in Fig. 43 show that COPs decreased gradually with the increase of the solar irradiance. However, the output voltage and current of the PV array and the battery bank increased with the increase of the solar irradiance.

In order to verify the correctness of the models, the operation characteristics of PV air-conditioning were tested during the period from 8:30 to 17:20 in June 29, 2015. The contrast results are shown in Figs. 44, 45, 46 and Table 23.

From Table 23, it can be observed that the simulated results are in a good agreement with the experimental values. The maximum relative errors of electricity

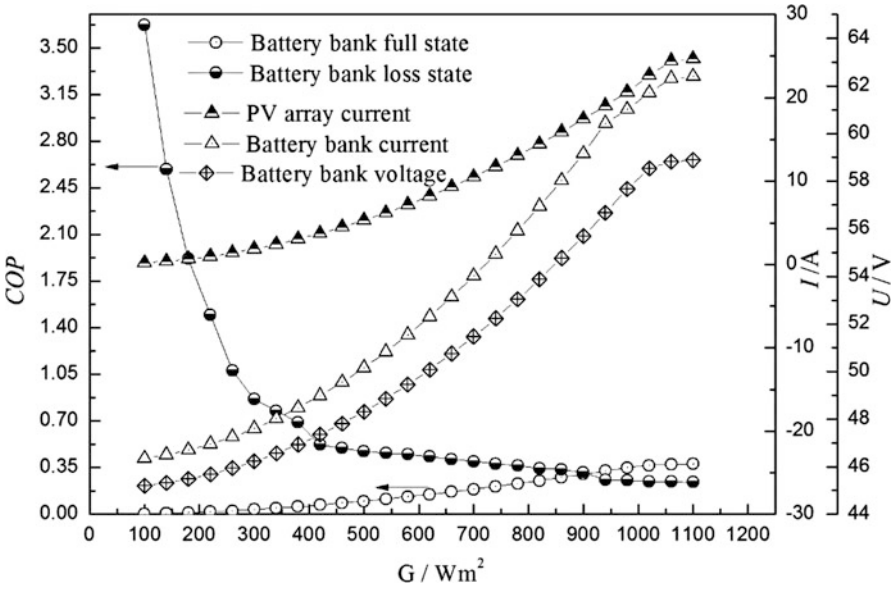

Fig. 43 Changes curves of COPs, as well as the output voltage and current of PV array and battery bank

power and COP between the simulated value and the measured results are 6.09% and 8.33%, respectively.

Conclusion

This chapter has introduced and studied four solar cooling systems, including adsorption absorption refrigerator, absorption refrigerator, photovoltaic refrigerator, and photovoltaic air-conditioning. The main conclusions are as follows:

1. A solar-powered finned-tube absorbent bed collector in solar adsorption cooling system was designed and optimized by increasing the internal fins and the mass transfer channel to enhance the heat and mass transfer in the collector. Some experiments on the adsorption/desorption process with and without valve control were made under four typical weather conditions, namely sunny and clear sky, sunny and partly cloudy sky, cloudy sky, and overcast sky. In the experiments, the maximum cooling efficiency was 0.122, and the daily maximum ice production was 6.5 kg. The cooling efficiency of the solar-powered adsorption refrigeration system with valve control in the adsorption/desorption process was significantly higher than that without valve control.
2. A 23 kW solar absorption cooling system was built. The collector was a parabolic trough solar collector (PTC), and a single-effect lithium bromide absorption chiller was employed in the cooling system. The cooling performance of the

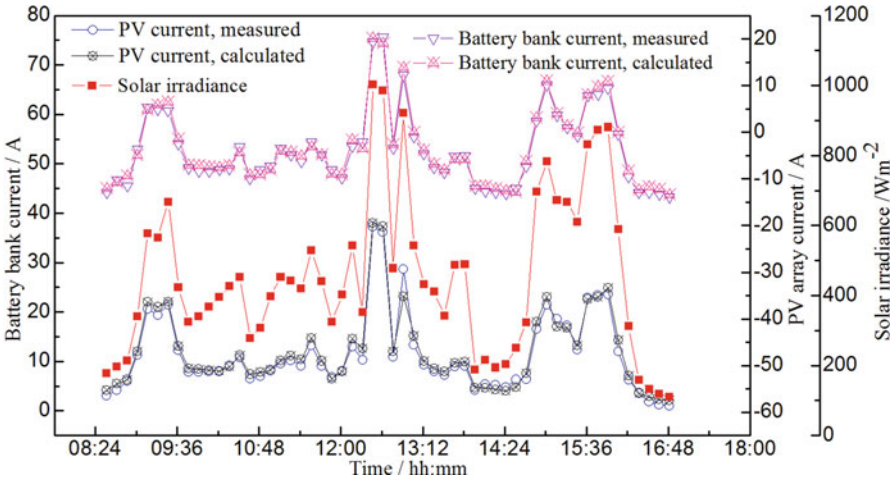

Fig. 44 Change curves of the output current and battery current of the PV module (measured value vs. calculated value)

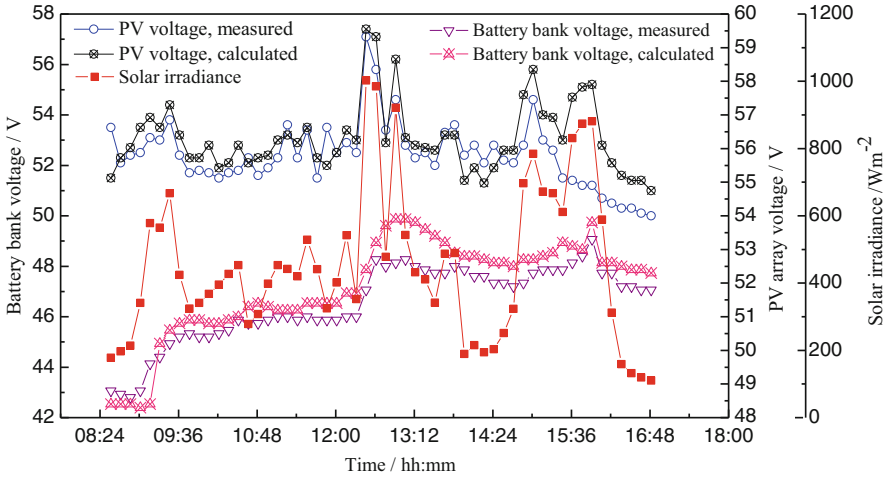

Fig. 45 Change curves of the output voltage and battery voltage of the PV module (measured value vs. calculated value)

single-effect LiBr-H_2O absorption chiller driven by PTC was investigated. The results uncover that the chiller's average refrigeration coefficient $\eta_{r,av}$ was between 0.18 and 0.60, and the average COP of the whole refrigeration cycle $COP_{s,av}$ was between 0.11 and 0.27 under different weather conditions. Moreover, the refrigeration quantity of the refrigeration chiller was increased with the increase of heat temperature. Meanwhile, the refrigeration coefficient also

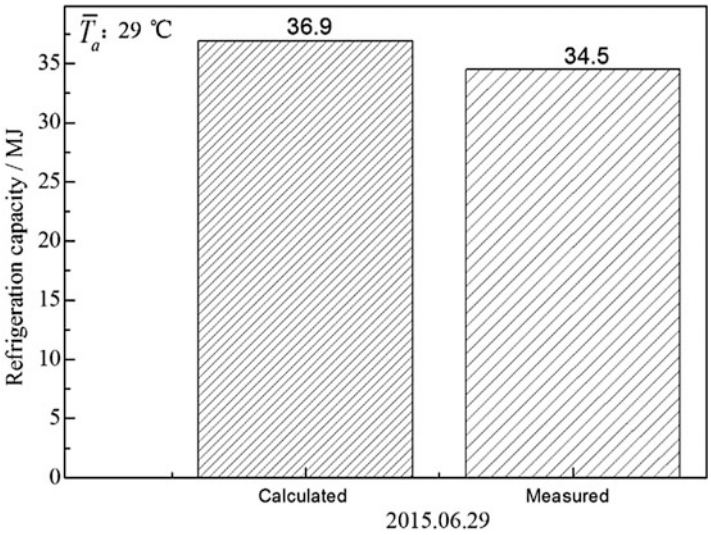

Fig. 46 Total energy derived from solar energy (measured value vs. calculated value)

Table 23 Comparison of experimental results and calculated values

	Electricity power (kW.h)		*COP*	
	Calculated	Measured	Calculated	Measured
Overcast day	4.8	4.5	0.3	0.3
Cloudy day	9.8	9.3	0.384	0.37
Sunny day	11.5	10.8	0.36	0.33

substantially increased with the rise of hot water temperature. The cooling water temperature could largely influence the performance of the refrigeration chiller.

3. A 112 L photovoltaic refrigerator was introduced, and its performance was investigated through an experiment. The operating performance of PV refrigerator was tested and analyzed on sunny days, cloudy days, and overcast days. The research results show that the system was mainly powered by the photovoltaic module on sunny days. It costed about 60 min for the temperature of the freezing room to reduce from the environment temperature to 0 °C. It took about 180 min for the temperature of the storage room to decline from the environment temperature to 5 °C. Furthermore, the voltage of the battery bank increased by 1.6 V, and the surplus electricity generated by the PV module was stored in the battery bank. On cloudy days, the system was powered by the photovoltaic module and the battery bank, and the voltage of the battery bank decreased by 1.5 V. It costed about 50 min for the temperature of the freezing room to reduce from the environment temperature to 0 °C. It took about 130 min for the temperature of the storage room to decline from the environment temperature to 5 °C. On overcast days, the system was mainly powered by the battery bank, and the

voltage of the battery bank decreased by 1.9 V. It took about 70 min for the temperature of the freezing room to reduce from the environment temperature to 0 °C. The temperature of the storage room costed about 150 min to decline from the environment temperature to 5 °C. Based on the experimental results about the load characteristics of the PV refrigerator, when the freezing room of the refrigerator was crammed with 5 kg, 6 kg, and 7 kg of water, respectively, it took about 791 min, 1151 min, and 1232 min to reach the setting temperature (−20 °C) of the freezing room correspondingly. The COP of the system was 0.24, 0.29, and 0.34, respectively.

4. The operating performance of the 1.5 HP photovoltaic air-conditioning system was tested for 1 year. On the basis of the investigation results, the maximum daily power generated by 2.4 kW PV array was about 8 kW·h. When the solar irradiance was higher than 675 W/m^2, the 1.5 HP steam compression type air-conditioning could be independently driven by the PV array. On sunny days, the air-conditioning system could be completely driven by the PV array for about 4 h per day. Focus was mainly put on cooling demand during the period from April to August. All the daily average COPs of the system were about 0.35, and its daily average guarantee rates were between 0.93 and 1.25.

References

1. Programme UNE (2012) Fifth Global Environmental Outlook Report (GEO-5)
2. Allouhi A (2015) Solar driven cooling systems: an updated review. Renew Sust Energ Rev 44:159–181
3. Ghafoor A, Munir A (2015) Worldwide overview of solar thermal cooling technologies. Renew Sust Energ Rev 43:763–774
4. Loh WS, El-Sharkawy II, Ng KC, Saha BB (2009) Adsorption cooling cycles for alternative adsorbent/adsorbate pairs working at partial vacuum and pressurized conditions. Appl Therm Energy 29(4):793–798
5. Wang LW, Wang RZ, Oliveira RG (2009) A review on adsorption working pairs for (2012) refrigeration. Renew Sust Energ Rev 13(3):518–534
6. Zhao YL, Hu E, Blazewicz A (2012) A non-uniform pressure and transient boundary condition based dynamic modeling of the adsorption process of an adsorption refrigeration tube. Appl Energy 90:280–287
7. Zhai XQ, Wang RZ (2010) Experimental investigation and performance analysis on a solar adsorption cooling system with/without heat storage. Appl Energy 87(3):824–835
8. Khattab NM, Sharawy H, Helmy M (2012) Development of vovel solar adsorption cooling tube. Energy Procedia 18:709–714
9. Attan D, Alghoul MA, Saha BB, Assadeq J, Sopian K (2011) The role of activated carbon fiber in adsorption cooling cycles. Renew Sust Energ Rev 15:1708–1721
10. Du S, Wang RZ, Xia ZZ (2015) Graphical analysis on internal heat recovery of a single stage ammonia–water absorption refrigeration system. Energy 80:687–694
11. Pan QW, Wang RZ, Lu ZS, Wang LW (2014) Experimental investigation of an adsorption refrigeration prototype with the working pair of composite adsorbent-ammonia. Appl Therm Energy 72:275–282
12. Xu ZY, Wang RZ (2014) Experimental verification of the variable effect absorption refrigeration cycle. Energy 77:703–709
13. Du S, Wang RZ, Xia ZZ (2014) Optimal ammonia water absorption refrigeration cycle with maximum internal heat recovery derived from pinch technology. Energy 68:862–869

14. Jiang L, Wang LW, Wang RZ (2014) Investigation on thermal conductive consolidated composite $CaCl_2$ for adsorption refrigeration. Int J Therm Sci 81:68–75
15. Ji X, Li M, Fan J, Zhang P, Luo B, Wang L (2014) Structure optimization and performance experiments of a solar-powered finned-tube adsorption refrigeration system. Appl Energy 113:1293–1300
16. Zhao YL, Hu E, Blazewicz A (2012) Dynamic modelling of an activated carbon–methanol adsorption refrigeration tube with considerations of interfacial convection and transient pressure process. Appl Energy 95:276–284
17. Rezk ARM, Al-Dadah RK (2012) Physical and operating conditions effects on silica gel/water adsorption chiller performance. Appl Energy 89:142–149
18. Louajari M, Mimet A, Ouammi A (2011) Study of the effect of finned tube adsorber on the performance of solar driven adsorption cooling machine using activated carbon–ammonia pair. Appl Energy 88(3):690–698
19. Karamanis D, Vardoulakis E (2012) Application of zeolitic materials prepared from fly ash to water vapor adsorption for solar cooling. Appl Energy 97:334–339
20. El-Sharkawy II, Saha BB, Koyama S, He J, Ng KC, Yap C (2008) Experimental investigation on activated carbon–ethanol pair for solar powered adsorption cooling applications. Int J Refrig 31(8):1407–1413
21. Saha BB, Koyama S, Lee JB et al (2003) Performance evaluation of a low-temperature waste heat driven multi-bed adsorption chiller. Int J Multiphase Flow 29(8):1249–1263
22. Saha BB, Akisawa A, Kashiwagi T (1997) Silica gel water advanced adsorption refrigeration cycle. Energy 22(4):437–447
23. Wang DC, JY W, Xia ZZ et al (2005) Study of a novel silica gel–water adsorption chiller. Part II. Experimental study. Int J Refrig 28(7):1084–1091
24. Wang DC, Xia ZZ, JY W et al (2005) Study of a novel silica gel–water adsorption chiller. Part I. Design and performance prediction. Int J Refrig 28(7):1073–1083
25. Critoph RE, Vogel R (1996) Possible adsorption pairs for use in solar cooling ambient. Energy 7 (4):183–190
26. Meunier F (1988) Theoretical performance of solid adsorbent cascading cycles using the zeolitewater and active carbon–methanol pairs: four cases studies. Heat Recovery Syst 6 (6):491–498
27. Kim DS, Infante Ferreira CA (2008) Solar refrigeration options- a state-of-the-art review. Int J Refrig 31:3–15
28. Iranmanesh A, Mehrabian MA (2013) Dynamic simulation of a single-effect LiBr-H_2O absorption refrigeration cycle considering the effects of thermal masses. Energ Buildings 60:47–59
29. Izquierdo M, González-Gil A, Palacios E (2014) Solar-powered single-and double-effect directly air-cooled LiBr-H_2O absorption prototype built as a single unit. Appl Energy 130:7–19
30. Lizarte R, Izquierdo M, Marcos JD, Palacios E (2013) Experimental comparison of two solar-driven air-cooled LiBr-H_2O absorption chillers: indirect versus direct air-cooled system. Energ Buildings 62:323–334
31. Agyenim F, Knight I, Rhodes M (2010) Design and experimental testing of the performance of an outdoor LiBr-H_2O solar thermal absorption cooling system with a cold store. Sol Energy 84:735–744
32. Lamine CM, Said Z (2014) Energy analysis of single effect absorption chiller (LiBr-H_2O) in an industrial manufacturing of detergent. Energy Procedía 50:105–112
33. González-Gil A, Izquierdo M, Marcos JD, Palacios E (2011) Experimental evaluation of a direct air-cooled lithium bromide–water absorption prototype for solar air conditioning. Appl Therm Eng 31:3358–3368
34. Li Z, Ye X, Liu J (2014) Performance analysis of solar air cooled double effect LiBr-H_2O absorption cooling system in subtropical city. Energy Convers Manag 85:302–312
35. Iranmanesh A, Mehrabian MA (2014) Optimization of a lithium bromide–water solar absorption cooling system with evacuated tube collectors using the genetic algorithm. Energ Buildings 85:427–435

36. López-Villada J, Ayou DS, Bruno JC, Coronas A (2014) Modelling, simulation and analysis of solar absorption power-cooling systems. Int J Refrig 39:125–136
37. Domínguez-Inzunza LA, Hernández-Magallanes JA, Sandoval-Reyes M, Rivera W (2014) Comparison of the performance of single-effect, half-effect, double-effect in series and inverse and triple-effect absorption cooling systems operating with the NH_3–$LiNO_3$ mixture. Appl Therm Eng 66:612–620
38. Li Z, Ye X, Liu J (2014) Optimal temperature of collector for solar double effect LiBr/H_2O absorption cooling system in subtropical city based on a year round meteorological data. Appl Therm Eng 69:19–28
39. Avanessian T, Ameri M (2014) Energy, exergy, and economic analysis of single and double effect LiBr-H_2O absorption chillers. Energ Buildings 73:26–36
40. Said SAM, El-Shaarawi MAI, Siddiqui MU (2015) Analysis of a solar powered absorption system. Energy Convers Manag 97:243–252
41. Fong KF, Chow TT, Lee CK, Lin Z, Chan LS (2011) Solar hybrid cooling system for high-tech offices in subtropical climate-radiant cooling by absorption refrigeration and desiccant dehumidification. Energy Convers Manag 52:2883–2894
42. Ketjoy N, yongphayoon R, Mansiri K (2013) Performance evaluation of 35 kW LiBr-H_2O solar absorption cooling system in Thailand. Energy Procedia 34:198–210
43. ZS L, Wang RZ, Xia ZZ, XR L, Yang CB, Ma YC et al (2013) Study of a novel solar adsorption cooling system and a solar absorption cooling system with new CPC collectors. Renew Energy 50:299–306
44. Ali AHH, Noeres P, Pollerberg C (2008) Performance assessment of an integrated free cooling and solar powered single-effect lithium bromide-water absorption chiller. Sol Energy 82:1021–1030
45. Hang Y, Qu M, Winston R, Jiang L, Widyolar B, Poiry H (2014) Experimental based energy performance analysis and life cycle assessment for solar absorption cooling system at University of Californian, Merced. Energ Buildings 82:746–757
46. Prasartkaew B (2014) Performance test of a small size LiBr-H_2O absorption chiller. Energy Procedia 56:487–497
47. Calise F, Palombo A, Vanoli L (2010) Maximization of primary energy savings of solar heating and cooling systems by transient simulations and computer design of experiments. Appl Energy 87:524–540
48. Dai YJ, Wang RZ, Ni L (2003) Experimental investigation and analysis on a thermoelectirc refrigerator driven by solar cells. Sol Energy Mater Sol Cells 77:377–391
49. Kaplanis S, Papanastasiou N (2006) The study and performance of a modified conventional refrigerator to serve as a PV powered one. Renew Energy 31:771–780
50. Aktacir MA (2011) Experimental study of a mufti-purpose PV-refrigerator system. Int J Phys Sci 6:746–757
51. Bilgili M (2011) Hourly simulation and performance of solar electric-vapor compression refrigeration system. Sol Energy 85:2720–2731
52. Modi A, Chaudhuri A, Vijay B, Mathur J (2009) Performance analysis of a solar photovoltaic operated domestic refrigerator. Appl Energy 86:2583–2591
53. Ekren O, Yilanci A, Cetin E, Ozturk HK (2011) Experimental performance evaluation of a PV-powered refrigeration system. Electron Electr Eng 114(8):7–10
54. Mba EF, Chukwuneke JL, Achebe CH (2012) Modeling and simulation of a photo-voltaic powered vapor compression refrigeration system. J Inf Eng Appl 2:1–15
55. Tina GM, Grasso AD (2014) Remote monitoring system for stand-alone photovoltaic power plants: the case study of a PV-powered outdoor refrigerator. Energy Convers Manag 78:862–871
56. Axaopoulos PJ, Theodoridis MP (2009) Design and experimental performance of a PV ice-maker without battery. Sol Energy 83:1360–1369

57. Navidbakhsh M, Shirazi A, Sanaye S (2013) Four E analysis and multi-objective optimization of an ice storage system incorporating PCM as the partial cold storage for air-conditioning applications. Appl Therm Eng 58:30–41
58. Pu J, Liu G, Feng X (2012) Cumulative exergy analysis of ice thermal storage air conditioning system. Appl Energy 93:564–569
59. Sanaye S, Shirazi A (2013) Thermo-economic optimization of an ice thermal energy storage system for air-conditioning applications. Energy Build 60:100–109
60. Sukamongkol Y, Chungpaibulpatana S, Ongsakul W (2002) A simulation model for predicting the performance of a solar photovoltaic system with alternating current loads. Renew Energy 27:237–258
61. Yang S M, Tao W Q (1998) Heat transfer. Beijing: Higher Education Press, Third Edition
62. Li J S, Yang Y Y (2001) Energy saving design for the door seal of the refrigerator. Household Electric Appliances 5(7):19–20
63. Dai Y J, Wang R Z, Ni L (2002) Experimental research and performance analysis of solar semiconductor refrigerator, Acta Energiae Solaris Sinica 23(6):754–758
64. Wei S B (1998) A new testing method for the refrigerator operating rate. Journal of Guangxi University for Nationalities (Natural Science Edition) 4(1):21–22
65. Bao J Q (2011) Low temperature preservation of food. Beijing: China Light Industry Press
66. Rabl A (1985) Active solar collectors and their applications. Oxford University Press, New York